Secondary gravity waves from the stratospheric polar vortex over ALOMAR Observatory on 12-14 January 2016: observations and modeling

Sharon L. Vadas[1], Erich Becker[1], Katrina Bossert[2], Gerd Baumgarten[3], Lars Hoffmann[4], and V. Lynn Harvey[5]

Keywords: Secondary gravity waves, lidar observations, polar vortex, AIRS observations, mountain waves

Submitted to JGR Atmospheres 4/21/2022, revised version submitted 10/27/22

• Main point #1: The upward and downward inertia GWs over ALOMAR are secondary GWs created by the breaking/dissipation of primary GWs from the polar vortex

• Main point #2: The primary GWs are created from imbalance of polar vortex and are amplified below the wind maximum where the vertical wind shear is large

• Main point #3: The primary and secondary GWs from the polar vortex simulated by the nudged HIAMCM agree well with lidar and AIRS observations

Plain Language Summary

Atmospheric gravity waves (GWs) are buoyancy driven perturbations in the Earth's atmosphere that can be created by various processes. GW breaking is similar to the breaking of an ocean wave when it overturns. A breaking GW imparts momentum to the atmosphere, which can create secondary GWs. We report on the long-period GWs observed by lidar over ALOMAR in northern Norway during 12-14 January 2016. We find that these GWs were secondary GWs created by the breaking of primary GWs, which in turn were generated by an imbalance of the polar vortex. We simulated this event with a GW-resolving global circulation model and directly compared the model results to ALOMAR lidar and AIRS satellite data. After we found that the model results agreed very well with these data, we investigated the simulated dynamics, which led to the interpretation about the origin of the observed ALOMAR GWs. This is the first model/data comparison study to show that GWs generated by the polar vortex are important to explain GWs observed in the Earth's winter mesosphere. This study also highlights the importance of the complicated process dubbed "multi-step vertical coupling" (MSVC), according to which secondary, not primary, are often observed in the wintertime mesosphere.

S. L. Vadas, NWRA, 3380 S. Mitchell Lane, Boulder, CO 80301, USA. (vasha@cora.nwra.com)

[1]Northwest Research Associates, Boulder,

Abstract.

We analyze the gravity waves (GWs) observed by a Rayleigh lidar at the Arctic Lidar Observatory for Middle Atmosphere Research (ALOMAR) (16.08° E, 69.38° N) in Norway at $z \sim 20-85$ km on 12-14 January 2016. These GWs propagate upward and downward away from $z_{\rm knee} = 57$ and 64 km at a horizontally-displaced location with periods $\tau_r \sim 5-10$ h and vertical wavelengths $\lambda_z \sim 9-20$ km. Because the hodographs are distorted, we in-

Colorado, USA

[2]Arizona State University 1. School of Earth and Space Exploration, 2. School of Mathematical and Statistical Sciences, Arizona State University, Tempe, AZ, USA

[3]Leibniz Institute of Atmospheric Physics at the University of Rostock, Kühlungsborn, Germany

[4]Jülich Supercomputing Centre, Forschungszentrum Jülich GmbH, Jülich, Germany

[5]Laboratory for Atmospheric and Space Physics, University of Colorado Boulder, Boulder, CO, USA

troduce an alternative method to determine the GW parameters. We find that these GWs are medium to large-scale, and propagate north/northwestward with intrinsic horizontal phase speeds of $\sim 35-65$ m/s. Since the GW parameters are similar above and below $z_{\rm knee}$, these are secondary GWs created by local body forces (LBFs) south/southeast of ALOMAR. We use the nudged HIAMCM (HIgh Altitude Mechanistic general Circulation Model) to model these events. Remarkably, the model reproduces similar GW structures over ALOMAR, with $z_{\rm knee}$ = 58 and 66 km. The event #1 GWs are created by a LBF at $\sim$ 35°E, $\sim$ 60°N and z $\sim$ 58 km. This LBF is created by the breaking and dissipation of primary GWs generated and amplified by the imbalance of the polar night jet below the wind maximum; the primary GWs for this event are created at $z \sim 25-35$ km at $49-53°$ N. We also find that the HIAMCM GWs agree well with those observed by the Atmospheric InfraRed Sounder (AIRS) satellite, and that those AIRS GWs south and north of $\sim$ 50°N over Europe are mainly mountain waves and GWs from the polar vortex, respectively.

1. Introduction

Atmospheric gravity waves (GWs) are created from many processes in the lower atmosphere, including wind flow over topography [*Watanabe et al.*, 2006; *Plougonven et al.*, 2008; *Alexander and Teitelbaum*, 2007, 2011; *Sato et al.*, 2012; *Smith et al.*, 2013; *Walterscheid et al.*, 2016; *Hoffmann et al.*, 2013, 2016; *Fritts et al.*, 2016, 2021; *Walterscheid et al.*, 2016; *Vadas and Becker*, 2019; *Becker and Vadas*, 2020; *Lund et al.*, 2020; *Hindley et al.*, 2021], deep convection [*Taylor and Hapgood*, 1988; *Fovell et al.*, 1992; *Alexander et al.*, 1995; *Holton and Alexander*, 1999; *Pandya*, 1999; *Piani et al.*, 2000; *Walterscheid et al.*, 2001; *Lane et al.*, 2001, 2003; *Beres et al.*, 2002; *Horinouchi et al.*, 2002; *Song et al.*, 2003; *Yue et al.*, 2009; *Vadas et al.*, 2009a, b; *Liu et al.*, 2014; *Stephan and Alexander*, 2015; *Holt et al.*, 2017; *Heale et al.*, 2019], geostrophic adjustment of the tropospheric jet [*Fritts and Luo*, 1992; *Luo and Fritts*, 1993; *Vadas and Fritts*, 2001; *Watanabe et al.*, 2008], and "spontaneous emission" from the polar vortex [*O'Sullivan and Dunkerton*, 1995; *Yoshiki and Sato*, 2000; *Yoshiki et al.*, 2004; *Zülicke and Peters*, 2006, 2008; *Sato and Yoshiki*, 2008; *Alexander et al.*, 2011; *Chen et al.*, 2013; *Plougonven and Zhang*, 2014; *Shibuya et al.*, 2017; *Dörnbrack et al.*, 2018; *Gassmann*, 2019; *Becker et al.*, 2022]. The amplitude of an upward-propagating GW increases approximately exponentially with height until the GW nears a critical level, breaks, or dissipates directly from molecular viscosity [*Hines*, 1960; *Pitteway and Hines*, 1963; *Fritts and Alexander*, 2003; *Vadas*, 2007]. (This increase is exactly exponential if the background wind and density scale height $\mathcal{H}$ are constant in altitude.) Upon breaking and dissipating, a GW packet deposits its energy and momentum into the background atmosphere, which creates a local body force (LBF) and heating that

excites a new set of GWs called secondary GWs [*Vadas et al.*, 2003, 2018; *Vadas and Liu*, 2009, 2013; *Becker and Vadas*, 2018; *Vadas and Becker*, 2018; *Heale et al.*, 2020]. If the primary wave packet is isolated when breaking and/or dissipating, the excited secondary GWs have horizontal wavelengths ranging from $\sim \lambda_H/4$ to several times the horizontal extent of the primary wave packet, where λ_H is the predominant horizontal wavelength of the primary GW packet. If, however, there is significant constructive/destructive interference between several wave packets from different sources at the breaking location, then the horizontal extent of the LBFs and heatings can be significantly smaller than λ_H of the primary GWs [*Vadas and Crowley*, 2010; *Vadas and Becker*, 2018, 2019]. These smaller-sized forces/heatings excite secondary GWs with significantly smaller horizontal wavelengths than λ_H of the primary GWs.

GW breaking also excites smaller-scale secondary GWs created by the non-linear interactions of the breaking process [*Satomura and Sato*, 1999; *Chun and Kim*, 2008; *Lane et al.*, 2003; *Snively and Pasko*, 2003; *Lund et al.*, 2020; *Heale et al.*, 2020]. Although most of these GWs have small horizontal phase speeds and are reabsorbed near the breaking region (and therefore contribute to the LBFs discussed above), some may propagate out of this region to higher altitudes [*Heale et al.*, 2020; *Fritts et al.*, 2021].

The temperature perturbations (as a function of z and time) of the secondary GWs excited by a LBF create a striking wave structure for a ground-observer at a horizontally-displaced location. These structures are dubbed "fishbone structures" [*Vadas et al.*, 2018], and are created because the secondary GW spectrum is rich, with different spectral components propagating at different speeds and ascent angles away from the LBF. (A GW's propagation angle with respect to the zenith in an isothermal windless background is

$\zeta = \cos^{-1}(\tau_B/\tau_{Ir})$, where τ_{Ir} is the GW intrinsic period and τ_B is the buoyancy period [*Vadas et al.*, 2009b]; thus high (low)-frequency GWs have steep (shallow) ascent angles.) A fishbone structure is asymmetric in z about the "knee" altitude $z_{\rm knee}$, which is the altitude of the horizontally-displaced LBF. This asymmetry consists of hot and cold GW phases meeting at $z_{\rm knee}$ whereby $T' = 0$. These secondary GWs consist of upward (downward)-propagating GWs having downgoing (upgoing) phases in time above (below) $z_{\rm knee}$, respectively, in a $z - t$ plot. (In this paper, upgoing/downgoing refers to the movement of a GW's phase in a $z - t$ plot, while upward/downward refers to the group velocity direction (i.e., propagation direction) of a GW.) In an isothermal, constant-wind atmosphere, the secondary GWs at the same distance above and below $z_{\rm knee}$ at a given time have the same horizontal wavelength λ_H, vertical wavelength λ_z, observed period τ_r, propagation direction, and density-scaled amplitude (e.g. $\sqrt{\overline{\rho}}T'$, where T' is the temperature perturbation and $\overline{\rho}$ is the background density). This fishbone structure is visible at any location except perpendicular to the LBF direction [*Vadas et al.*, 2003, 2018].

Two fishbone structures containing secondary GWs were identified in wintertime lidar data at McMurdo on 18 June 2014 and 29 June 2011 with $z_{\rm knee} = 43$ and 52 km, respectively [*Vadas et al.*, 2018]. These were inertia GWs with periods of $\tau_r \sim 6 - 10$ hrs and $|\lambda_z| \sim 6 - 14$ km. Additionally, fishbone structures containing medium to large-scale inertia GWs were identified in simulation data with $z_{\rm knee} = 35 - 60$ km at McMurdo [Fig. 5 of *Vadas and Becker*, 2018]. These latter GWs had the same density-scaled amplitudes, λ_H, λ_z, τ_r, and propagation direction above and below $z_{\rm knee}$, and were therefore identified as secondary GWs. The LBF which excited these GWs was created from the breaking of primary GWs from below [Fig. 18-22 of *Vadas and Becker*, 2018].

While the McMurdo study of *Vadas et al.* [2018] contains the only published cases of secondary GWs in fishbone structures that we are aware of, there have been other high latitude lidar studies where upward and downward-propagating inertia GWs have been observed. *Baumgarten et al.* [2015] and *Strelnikova et al.* [2020] observed persistent inertia GWs at ALOMAR in the stratosphere and mesosphere having upgoing and downgoing phases in time, indicating the possible presence of downward and upward-propagating secondary GWs, respectively. *Kaifler et al.* [2017] observed upward and downward-propagating inertia GWs at $z \sim 50$ km on 6 December 2015 using a Rayleigh lidar in Finland (Fig. 8 of that work). They wrote "Remarkably, upward [upgoing] phase progression waves are found below 50 km and downward [downgoing] phase progression waves above. [...] Vertical wavelengths of downward [downgoing] and upward [upgoing] phase progression waves at ~ 50 km altitude are in the same range (10-12 km, Fig.8f)". They also found that the wave periods were similar above and below $z \sim 50$ km, $\tau_r \sim 7 - 8$ h (Fig. 8e of that work), and that the GWs with upgoing phases were downward-propagating GWs. These downward GWs could not have been reflected waves, because reflection occurs when $m \to 0$ or $|\lambda_z| \to \infty$ whereby the phase lines become vertical, which was not observed. Here, $m = 2\pi/\lambda_z$. These GWs may have been secondary GWs created by a horizontally-displaced LBF at $z \sim 50$ km.

In fact, inertia GWs are often observed in the wintertime high latitude stratosphere and mesosphere. These observations have occurred over McMurdo [*Chen et al.*, 2013, 2016; *Chen and Chu*, 2017; *Zhao et al.*, 2017], Syowa Station [*Shibuya et al.*, 2017], ALOMAR [*Baumgarten et al.*, 2015; *Strelnikova et al.*, 2020], Kühlungsborn Germany [*Strelnikova et al.*, 2021], Alaska [*Nicolls et al.*, 2010; *Li et al.*, 2021], and at the Andes Lidar Obser-

vatory [*Huang et al.*, 2017]. Such inertia GWs could be secondary or higher-order GWs from orographic forcing [*Becker and Vadas*, 2018; *Vadas and Becker*, 2018].

Are there other sources for wintertime inertia GWs? *Bossert et al.* [2020] analyzed the temperature perturbations in AIRS over Europe during January 2016. Although mountain waves (MWs) were visible at midlatitudes (e.g., over the Alps), their study suggested that the high-latitude GWs at $z \sim 30 - 45$ km may have been created by the stratospheric polar vortex. *Dörnbrack* [2021] disputed this interpretation, instead arguing that these high-latitude waves were trailing MWs from the Alps due to the blended nature of the phase lines at $z \sim 40$ km. A recent modeling paper using the HIAMCM showed that the polar vortex created inertia GWs during January 2016 [*Becker et al.*, 2022, hereafter B22]. That study showed that these GWs were amplified by the transfer of kinetic energy from the large-scale flow to the GWs in a process found to be strongest where the vertical shear of the horizontal wind (hereafter vertical wind shear) was maximum in the middle stratosphere. This amplification process typically occurs at the outer edge of the polar vortex below the altitude where the horizontal wind is the largest. This region allows for the greatest extraction of energy from the mean flow into the generated GWs. B22 also showed that there was a persistent GW hot spot over Europe during January 2016, and that the HIAMCM results agreed well with AIRS data during that month.

In this paper, we investigate the GWs in the fishbone structures observed by a Rayleigh lidar over ALOMAR on 12-14 January 2016. In Section 2, we review the GW dispersion and polarization relations. We analyze the GWs observed by the ALOMAR lidar in Section 3. Since the hodographs are distorted, we develop an alternative method to determine the GW intrinsic parameters using the GW dispersion and polarization rela-

tions. In Section 4, we model these events using the nudged HIAMCM, and compare the results with lidar and AIRS data. Because good agreement is obtained, we analyze the HIAMCM results to determine the multi-step vertical coupling that created the GWs over ALOMAR. Section 5 contains our conclusions. Appendix A calculates the fishbone structure for multiple LBFs, and Appendix B compares the GWs in the HIAMCM and AIRS over the Atlantic Ocean during this time period.

2. Parameters and Phase/Amplitude Relationships of a GW

2.1. Gravity Wave Dispersion and Polarization Relations

The general fluid equations are fully compressible, and include GWs and acoustic waves (AWs). Several approximations are commonly employed if $|\lambda_z|$ is not too large, such as the Boussinesq and anelastic approximations. Earth's rotation is included for inertia GWs with intrinsic periods $\tau_{Ir} > 4$ h at mid and high latitudes by employing the f-plane approximation, where the latitude is assumed fixed. If the background atmosphere is locally-constant and the perturbations are linear, analytic solutions can be obtained. These are the GW dispersion and polarization relations, which govern how the wavenumber, amplitude and phase of a GW changes as it propagates. The general non-dissipative relations were derived by *Hines* [1960] (dispersion relation) and *Vadas* [2013] (polarization relations). These expressions are also applicable to a GW in the thermosphere below the altitude where molecular viscosity begins to significantly damp it [*Vadas*, 2007].

The altitude where molecular viscosity becomes important for significantly damping a GW depends sensitively on λ_z and the intrinsic horizontal phase speed, $c_{IH} = \partial\omega_{Ir}/\partial k_H$, where ω_{Ir} is the intrinsic frequency and $k_H = 2\pi/\lambda_H$ [*Vadas*, 2007]. This damping becomes

significant when the following expression is satisfied:

$$\frac{\lambda_z^3 \omega_{Ir}}{8\pi^3 \mathcal{H}(1+\mathrm{Pr}^{-1})} \sim \nu(z) \tag{1}$$

[Eq.(9) of *Vadas and Liu*, 2009], where $\nu(z) = \mu/\overline{\rho}$ is the kinematic viscosity, μ is the molecular viscosity, $\overline{\rho}$ is the background density, Pr is the Prandtl number, and $\mathcal{H}$ is the density scale height. In the thermosphere, Pr $\simeq 0.62$ [*Banks and Kockarts*, 1973b; *Vadas and Crowley*, 2017]. Small-λ_z GWs are damped near the turbopause at $z \sim 107$ km. Because ν increases exponentially in z, every GW is eventually damped by viscosity, wherein the changes of its wavenumber, amplitude and phase are described by the viscous dispersion and polarization relations [e.g., *Vadas and Fritts*, 2005; *Vadas and Nicolls*, 2012].

The compressible, f-plane, non-dissipative dispersion relation for GWs and AWs is

$$\omega_{Ir}^4 - [f^2 + c_s^2(\mathbf{k}^2 + 1/4\mathcal{H}^2)]\omega_{Ir}^2 + c_s^2[k_H^2 N_B^2 + f^2(m^2 + 1/4\mathcal{H}^2)] = 0 \tag{2}$$

[*Hines*, 1960]. Here, $\omega_{Ir} = 2\pi/\tau_{Ir}$ is the intrinsic frequency:

$$\omega_{Ir} = \omega_r - (k\overline{U} + l\overline{V}), \tag{3}$$

$\omega_r = 2\pi/\tau_r$ is the ground-based frequency, $\overline{U}$ and $\overline{V}$ are the zonal and meridional components of the background wind, respectively, k, l, and m are the zonal, meridional and vertical wavenumbers, respectively, $k_H = \sqrt{k^2 + l^2} = 2\pi/\lambda_H$, $m = 2\pi/\lambda_z$, $\mathbf{k}^2 = k^2 + l^2 + m^2$, $\mathcal{H} = -\overline{\rho}/(d\overline{\rho}/dz)$ is the density scale height, $N_B = \sqrt{\gamma - 1}\, g/c_s$ is the buoyancy frequency, $c_s = \sqrt{\gamma g \mathcal{H}}$ is the sound speed, $f = 2\Omega \sin\theta$, $\Omega = 2\pi/24\,\mathrm{hr}$ is Earth's rotation rate, θ is the latitude, $g = 9.8(R_\mathrm{E}/(R_\mathrm{E}+z))^2$ is the acceleration due to gravity and $R_\mathrm{E} = 6.371 \times 10^6$ m is Earth's radius. Note that $m < 0$ ($m > 0$) for an upward (downward)-propagating GW, assuming $\omega_{Ir} > 0$ without loss of generality. In addition, $\gamma = 1 + \mathrm{r}/C_v = C_p/C_v$,

203 $\mathrm{r} = (8308/\mathrm{X_{MW}})\,\mathrm{m^2 s^{-2} K^{-1}}$, $\mathrm{X_{MW}}$ is the mean molecular weight, and C_v (C_p) is the mean
204 specific heat at constant volume (pressure). If the dominant molecule(s) is diatomic
205 (monatomic), $\gamma = 1.4$ ($\gamma = 1.667$). Simple empirical expressions for $\mathrm{X_{MW}}$ and γ are

$$\mathrm{X_{MW}} = \frac{1}{2}(\mathrm{X_{MW0}} - \mathrm{X_{MW1}})\left(1 - \tanh\left(\frac{\mathrm{s-a}}{\Delta_a}\right)\right) + \mathrm{X_{MW1}} \quad (4)$$

$$\gamma = \frac{1}{2}(\gamma_0 - \gamma_1)\left(1 - \tanh\left(\frac{\mathrm{s-b}}{\Delta_b}\right)\right) + \gamma_1, \quad (5)$$

206 respectively, where $\mathrm{s} = -\ln(\overline{\rho})$ ($\overline{\rho}$ has units of $\mathrm{g/m^3}$), $\mathrm{X_{MW0}} = 28.9$, $\mathrm{X_{MW1}} = 16$, $\mathrm{a} = 14.9$,
207 $\Delta_a = 4.2$, $\gamma_0 = 1.4$, $\gamma_1 = 1.667$, $\mathrm{b} = 15.1$ and $\Delta_b = 4.0$ [Eqs. (3-4) of *Vadas*, 2007].

208 The GW dispersion relation is obtained from the smaller root from Eq. (2):

$$\omega_{Ir}^2 = \frac{a}{2}\left[1 - \sqrt{1 - 4b/a^2}\right], \quad (6)$$

209 where

$$a = [f^2 + c_s^2(\mathbf{k}^2 + 1/4\mathcal{H}^2)], \quad (7)$$

$$b = c_s^2[k_H^2 N_B^2 + f^2(m^2 + 1/4\mathcal{H}^2)] \quad (8)$$

210 [Eqs. (31), (33), (34) of *Vadas*, 2013]. If a GW propagates much slower than c_s
211 ($\omega_{Ir}/\sqrt{\mathbf{k}^2 + 1/4\mathcal{H}^2} \ll c_s$), Eq. (6) reduces to the usual anelastic GW dispersion rela-
212 tion:

$$\omega_{Ir}^2 = \frac{k_H^2 N_B^2 + f^2(m^2 + 1/4\mathcal{H}^2)}{m^2 + k_H^2 + 1/4\mathcal{H}^2} \quad (9)$$

213 [*Marks and Eckermann*, 1995]. Then $\lambda_H = 2\pi/k_H$ can be determined via

$$k_H^2 = \frac{(\omega_{Ir}^2 - f^2)(m^2 + 1/4\mathcal{H}^2)}{N_B^2 - \omega_{Ir}^2}. \quad (10)$$

214 Assuming plane wave solutions of the form

$$(\mathrm{e}^{-z/2\mathcal{H}}u')(x,y,z,t) = \mathrm{e}^{i(\omega_r t - kx - ly - mz)}(\widetilde{\mathrm{e}^{-z/2\mathcal{H}}u'})(k,l,m), \quad (11)$$

where the widetilde " ~ " denotes taking the Fourier transform of all factors within the parentheses in space and time, the compressible GW polarization relations are

$$\hat{v} = \frac{il\omega_{Ir} - fk}{ik\omega_{Ir} + fl}\hat{u} \tag{12}$$

$$\hat{w} = \frac{-\omega_{Ir}(m - \frac{i}{2\mathcal{H}} + \frac{i}{\gamma\mathcal{H}})(\omega_{Ir}^2 - f^2)(k\omega_{Ir} + ifl)}{(N_B^2 - \omega_{Ir}^2)(k^2\omega_{Ir}^2 + f^2l^2)}\hat{u}, \tag{13}$$

$$\hat{T} = \frac{N_B^2(im - \frac{1}{2\mathcal{H}}) - \frac{\omega_{Ir}^2}{\gamma\mathcal{H}}(1-\gamma)}{g\omega_{Ir}(m - \frac{i}{2\mathcal{H}} + \frac{i}{\gamma\mathcal{H}})}\hat{w}, \tag{14}$$

$$\hat{w} = \frac{-(m - \frac{i}{2\mathcal{H}} + \frac{i}{\gamma\mathcal{H}})(\omega_{Ir}^2 - f^2)}{(N_B^2 - \omega_{Ir}^2)k_H}\hat{u}_H \tag{15}$$

[Eqs. (B3), (B8) and (B11) of *Vadas*, 2013] and [Eq.(42) of *Vadas et al.*, 2018]. Here, the "hatted" quantities are the Fourier transforms of the density-scaled perturbations:

$$\hat{u} = (\widetilde{e^{-z/2\mathcal{H}}u'}), \qquad \hat{v} = (\widetilde{e^{-z/2\mathcal{H}}v'}), \qquad \hat{u}_H = (\widetilde{e^{-z/2\mathcal{H}}u'_H}), \tag{16}$$

$$\hat{w} = (\widetilde{e^{-z/2\mathcal{H}}w'}), \qquad \hat{T} = (\widetilde{e^{-z/2\mathcal{H}}T'/\overline{T}}), \tag{17}$$

where u', v' and w' are the GW zonal, meridional and vertical velocity perturbations, respectively, $u'_H = \sqrt{(u')^2 + (v')^2}$, T' is the temperature perturbation, and $\overline{T}$ is the background temperature. If we assume the sign convection $e^{i(-\omega_r t + kx + ly + mz)}$ instead of the RHS of Eq. (11), then one must replace i by $-i$ in Eqs. (12)-(15) to obtain the corresponding polarization relations. (Note that the chosen sign convention does not affect the physically-observed atmospheric perturbations.) Eqs. (12)-(15) yield the phase and amplitude relationships between u', v', w', u'_H and T'. For example,

$$\hat{T} = (\alpha + i\beta)\hat{w} = A\exp(i\zeta)\hat{w}, \tag{18}$$

where $A = \sqrt{\alpha^2 + \beta^2}$ and $\zeta = \tan^{-1}(\beta/\alpha)$. Then the phase shift between $\hat{T}$ and $\hat{w}$ is ζ and the amplitude ratio is A. If $|\lambda_z| \ll 4\pi\mathcal{H}$, then u', v', w', u'_H and T' can be substituted in for $\hat{u}$, $\hat{v}$, $\hat{w}$, $\hat{u}_H$ and $\hat{T}$, respectively, in Eqs. (12)-(15).

2.2. Hodograph solutions for a gravity wave

Multiplying Eq. (12) by its complex conjugate yields

$$\left(l^2\omega_{Ir}^2 + f^2k^2\right)|\hat{u}|^2 - \left(k^2\omega_{Ir}^2 + f^2l^2\right)|\hat{v}|^2 = 0, \tag{19}$$

where "$*$" denotes the complex conjugate and $|\hat{u}|^2 = \hat{u}\hat{u}^*$, for example. We define the GW propagation direction in the horizontal plane counter-clockwise from east as ψ. Then

$$k = k_H \cos\psi, \qquad l = k_H \sin\psi. \tag{20}$$

Plugging Eq. (20) into Eq. (19), we get

$$\left[1 + \left(\frac{\omega_{Ir}}{f}\right)^2 \tan^2\psi\right]|\hat{u}|^2 - \left[\left(\frac{\omega_{Ir}}{f}\right)^2 + \tan^2\psi\right]|\hat{v}|^2 = 0. \tag{21}$$

We rotate to a coordinate system parallel to the GW propagation direction so that $\hat{u}_\parallel$ and $\hat{u}_\perp$ are the parallel (long axis) and perpendicular (short axis) components of the horizontal wind perturbations, respectively. Setting $\psi = 0$ in this system, Eq. (21) becomes

$$|\hat{u}_\parallel|^2 = \left(\frac{\omega_{Ir}}{f}\right)^2 |\hat{u}_\perp|^2. \tag{22}$$

If $|\lambda_z| \ll 4\pi\mathcal{H}$, $\hat{u}_\parallel = u'_\parallel$ and $\hat{u}_\perp = u'_\perp$ so that

$$|u'_\parallel|^2 = \left(\frac{\omega_{Ir}}{f}\right)^2 |u'_\perp|^2. \tag{23}$$

Eq. (23) shows that the ratio of the parallel to the perpendicular lengths of the ellipse formed by plotting u' versus v' for a GW yields ω_{Ir}/f via the hodograph method, as is well known [e.g., *Sawyer*, 1961; *Cot and Barat*, 1986; *Wang and Geller*, 2003; *Zhang et al.*, 2004; *Chen et al.*, 2013; *Baumgarten et al.*, 2015; *Strelnikova et al.*, 2020]. Additionally, because the GW propagation direction is parallel to the long axis of the ellipse, ψ is determined from the hodograph except for a 180° ambiguity. This ambiguity is eliminated

by using the phase shift between T' and u' (or v') [e.g., *Chen et al.*, 2013; *Baumgarten et al.*, 2015]. λ_H is then determined from the GW dispersion relation when λ_z is measured.

3. Observations and Analysis of Fishbone Structure GWs at ALOMAR

3.1. RMR Lidar observations at ALOMAR

We make use of temperature and wind data acquired with the Doppler Rayleigh-Mie-Raman (RMR) lidar installed at the Arctic Lidar Observatory for Middle Atmosphere Research (ALOMAR), located in northern Norway at 69.38° N, 16.08° E. This lidar measures temperatures and winds during daytime and nighttime [e.g., *von Zahn et al.*, 2000; *Schöch et al.*, 2008; *Fiedler et al.*, 2011; *Baumgarten et al.*, 2015]. Two lasers emit pulses in two different directions with a zenith distance angle of 20°. The azimuths for the north and east viewing telescopes are 0° and 90°, respectively. The backscattered photons are collected by two receiving telescopes. One single detection system is used for recording the backscattered light (among others) at wavelengths of 355 nm and 532 nm, where the latter is further analyzed with a Doppler Iodine Spectrometer [*Baumgarten*, 2010]. These backscattered signals are used to calculate the temperature profiles [*Hauchecorne and Chanin*, 1980]. The wind is measured in the zonal and meridional directions given by the pointing of the two outgoing beams and the viewing direction of the telescopes. From the measured Doppler-shift, the horizontal wind is calculated assuming negligible contribution from the vertical wind.

The temperature profiles are available up to 90 km during the nighttime and 70 km during the daytime. The (oversampled) data is available with a resolution of 5 min and 150 m. This data allows for the detection of waves down to periods of 1 hour and vertical wavelengths of 1 km. We interpolate over missing data or data that have values which

significantly deviate from the mean. We do not use data below 25 km due to uncertainties introduced by the stratospheric aerosol layer and the presence of polar stratospheric clouds [*Baumgarten*, 2010; *Langenbach et al.*, 2019].

3.2. Extraction of fishbone structures from the lidar data

Fig. 1a shows a time-height cross section of the scaled temperature perturbation, $T' \exp(-z/14\text{km})$, and Fig. 1b shows the background mean temperature, $\overline{T}$, from the lidar at ALOMAR on 12-14 January 2016. Here, we use Fourier filtering to obtain the perturbations, which have $1 \leq \tau_r \leq 11$ h so that the semi-diurnal and diurnal tides are removed and $|\lambda_z| \geq 1$ km. Note that $\tau_r \geq 1$ h and $|\lambda_z| \geq 1$ km are consistent with the requirement for extracting waves from the lidar data (see Sec. 3.1). Because $\exp(-z/14\text{km})$ is roughly the square root of the background density (since $\mathcal{H} \sim 7$ km), multipying T' by this factor causes the amplitudes of the upward and downward-propagating GWs in the fishbone structures to be the same if $\overline{T}$, $\overline{U}$ and $\overline{V}$ are constant, and therefore enables easier identification of these structures. Fig. 1c-d show the scaled zonal and meridional wind perturbations, $u' \exp(-z/14\text{km})$ and $v' \exp(-z/14\text{km})$, respectively. Two fishbone structures are observed in Fig. 1: events #1 and 2 (black arrows). Note that these structures are not as "clean" as in *Vadas et al.* [2018] because of constructive/destructive interference of the main fishbone GWs with "contaminant" GWs. (As we find in Sec. 4 and Appendix A, these contaminant GWs are secondary GWs from neighboring LBFs.)

Fig. 2a-b show $T' \exp(-z/14\text{km})$ for GWs with upgoing and downgoing phases in time, respectively, obtained by taking the Fourier transform of Fig. 1a. Upgoing phase lines (suggesting downward-propagating GWs) are only visible below $z \sim 60$ km and 66 km during events #1 and #2, respectively. There is a corresponding decrease or dip in

amplitude for the downgoing phase lines (suggesting upward-propagating GWs) in Fig. 2b at $z \sim 60$ km and 66 km during events #1 and #2, respectively. These results suggest that in-situ upward and downward-propagating GWs are generated at these altitudes.

We determine $z_{\rm knee}$ as follows. We first locate the altitude range where the amplitudes of the filtered upgoing phase lines (downward GWs) in Fig. 2a become quite small. This is the altitude range where the downward secondary GWs are created. During event #1, this altitude range is estimated to be $z \sim 54 - 60$ km from Fig. 2a. We outline this downward-GW generation region with a pink dash rectangle in Fig. 2a, and duplicate this rectangle in Fig. 1a. We now use the fact that $T' = 0$ for the secondary GWs at $z_{\rm knee}$, which is the altitude of a (horizontally-displaced) LBF [*Vadas et al.*, 2003, 2018]. We then estimate the average altitude within the GW generation region (pink rectangle) where the hot and cold upgoing and downgoing phase lines meet in Fig. 1a, and define this altitude to be $z_{\rm knee}$. Examining the upgoing and downgoing phase lines within the event #1 pink rectangle in Fig. 1a, we estimate an average altitude where the hot and cold phase lines meet of $z \sim 57$ km; therefore we set $z_{\rm knee} = 57$ km for event #1.

For event #2, the amplitude of the upgoing phase lines are quite small at $z \sim 60 - 65$ km (event #2 pink dash rectangle) in Fig. 2a. Examining this same altitude range in Fig. 1a, we estimate an average altitude where the hot and cold phase lines meet of $z \sim 64$ km; therefore we set $z_{\rm knee} = 64$ km for event #2. The arrows in Fig. 2a point directly at $z_{\rm knee}$. Note that constructive/destructive interference with secondary GWs from neighboring LBFs makes it more difficult to determine $z_{\rm knee}$ for the main fishbone structures (see Appendix A). Additionally, saturation of the primary GWs smears T' at $z_{\rm knee}$, thereby making it more difficult to determine $z_{\rm knee}$ of the secondary GWs. We

overplot in Fig. 2 the knee altitudes $z_{\rm knee} = 57$ km before 13.7 January and $z_{\rm knee} = 64$ km after 13.7 January (dashed line). As a consistency check, we note that nearly all of the scaled amplitudes for GWs with downgoing phases decrease near the dashed line in Fig. 2b after 13.2 January. (Here, 13.2 January refers to ∼5 UT on 13 January.)

Note that the event #1 (#2) GWs with downgoing phases (suggesting upward-propagating GWs) in Fig. 2b are damped at $z \sim 65 - 70$ km ($z \sim 72 - 78$ km); this damping must be caused by wave breaking that is induced by amplitude growth (instead of refraction by the background wind) since λ_z is relatively constant during the damping.

Boundaries that enclose relatively "clean" fishbone structures from Figs. 1-2 are as follows. Event #1 is chosen to be at $45 < z < 75$ km on 13.1-13.6 January, and event #2 is chosen to be at $48 < z < 80$ km on 13.7-14.2 January. Fig. 2c shows those GWs with downgoing (upgoing) phases above (below) the dashed line for the chosen time and altitude boundaries. Fishbone structures are seen during events #1 and 2. Note that the hot-cold phases do not always line up due to the presence of contaminant waves.

The second and third rows of Fig. 2 show the corresponding results for u' and v'. Note that large-amplitude GWs not part of the fishbone structure propagate upward from below through event #1 in Fig. 2e (purple arrow). Therefore, we do not show the GWs with downgoing phase lines above $z_{\rm knee}$ during event #1 for u' in Fig. 2f.

3.3. Estimation of the intrinsic parameters of the lidar GWs from the hodograph method

Fig. 3a-b show the PSD (power spectral density) of T' from Fig. 2c, $[\widetilde{T'}]^2$, above and below the knee, respectively, calculated within the time and altitude boundaries for event #1. Here we show the PSD of T' instead of u'_H because we have complete T' data above

and below $z_{\rm knee}$ for both events (see 3rd column of Fig. 2). The peak values are $|\tau_r| \sim 5-8$ h and $|\lambda_z| \sim 10-20$ km. Since $|\tau_r|$ and $|\lambda_z|$ are similar above and below $z_{\rm knee}$, these GWs are likely secondary GWs from a horizontally-displaced LBF at $z_{\rm knee} = 57$ km. We fit 2D Gaussian functions to the PSD to obtain best-fit values below $z_{\rm knee}$ for $|\lambda_z|$ and $|\tau_r|$; the results are shown in Table 1.

Fig. 3c shows the lidar perturbations u', v' and $(g/N_B)T'/\overline{T}$ as functions of time at $z = 54$ km via setting $N_B = 0.02\,$rad/s and $g = 9.8(R_{\rm E}/(R_{\rm E}+z))^2 = 9.6\,{\rm m/s^2}$. Figs. 3d-e show temporal and altitudinal hodographs, respectively. The hodographs rotate counter-clockwise in time and altitude, thereby implying that the GWs below $z_{\rm knee}$ propagate downward in time. These hodographs are distorted ellipses due to the presence of contaminant GWs which create "checkerboard" patterns in T' at $45 < z < 57$ km and at 13.1-13.6 January in Fig. 2c,f,i. These contaminant GWs are likely secondary GWs from neighboring LBFs (see Sec. 4).

We roughly estimate $u'_{\parallel} \sim 21$m/s, $u'_{\perp} \sim 4$m/s, and $u' \sim 17$m/s from Fig. 3d, where u' is the total zonal velocity perturbation (i.e., the projection of the hodograph onto the u' axis). Using Eqs. (10) and (23), $|\lambda_z| = 15$ km and $2\pi/f = 12.8$ h, we estimate $\tau_{Ir} = 2\pi/\omega_{Ir} \sim 2.4$ h and $\lambda_H = 421$ km. Using Eq. (20), $\psi = \cos^{-1}(u'/u'_{\parallel})$, which yields northwest or southeast propagation directions of $\psi \sim 144^\circ$ or -36°.

Fig. 4a shows the wind from NASA's Modern-Era Retrospective analysis for Research and Applications, Version 2 (MERRA-2) reanalysis data [*Gelaro et al.*, 2017] on 13.0 January at $z = 48$ km, which is the height where the polar night jet has a maximum speed of $\rm U_{tot} = 133$m/s, where $\rm U_{tot} = \sqrt{\overline{U}^2 + \overline{V}^2}$. The jet is strong over the Atlantic Ocean and northern Europe. We overplot the vortex edge (white line) using the streamfunction

method of *Harvey et al.* [2002]. The vortex edge roughly follows the poleward flank of the wind maximum. Fig. 4b-c show the horizontal wind at $z = 54$ and 58 km. Below $z_{\rm knee}$ during event #1, the wind is mainly eastward at ALOMAR (asterisk). If the event #1 GWs propagated northwestward (southeastward), they would have propagated mainly against (with) the wind, which would have resulted in $\tau_{Ir} < |\tau_r|$ ($\tau_{Ir} > |\tau_r|$) from the Doppler shift. Since $\tau_{Ir} < |\tau_r|$, the event #1 GWs must have propagated northwestward.

Fig. 3f-j and Table 1 show the corresponding results for event #2. Since $|\tau_r|$ and $|\lambda_z|$ are similar above and below $z_{\rm knee}$, these GWs are likely secondary GWs. While the hodograph in Fig. 3j rotates counter-clockwise in z, the hodograph in Fig. 3i rotates both clockwise and counter-clockwise in time due to the presence of contaminant GWs (see Figs. 3h-j and 2c,f,i), thereby yielding an ambiguous result. We roughly estimate $u'_{\parallel} \sim 7$m/s, $u'_{\perp} \sim 4$m/s, and $u' \sim 3$m/s. Using Eq. (23), we estimate $\tau_{Ir} = 2\pi/\omega_{Ir} \sim 7.3$ h and $\psi = 115^\circ$ or -65°.

Fig. 4d shows the wind on 13.5 January at $z = 48$ km, the height where the polar vortex has a maximum speed of $U_{\rm tot} = 156$m/s, and Fig. 4e-f show the wind at $z = 54$ and 64 km. Below $z_{\rm knee}$ during event #2, the wind is mainly eastward at ALOMAR. If the event #2 GWs propagated northward or southward, they would have propagated approximately perpendicular to the wind direction, so that $\tau_{Ir} \simeq \tau_r$. Because T' peaks before u' in Fig. 3h, we show in Sec. 3.4 that these GWs propagated northward.

3.4. Alternative method to determine the intrinsic parameters of lidar GWs

The hodograph method used in Sec. 3.3 is the usual way to determine the intrinsic parameters of inertia GWs from lidar data. However, because of contamination from other GWs, we were only able to obtain rough estimates of these parameters. We now

present an alternative method to obtain the best-fit intrinsic GW parameters and 1−sigma errors using the GW polarization and dispersion relations.

To motivate this method, Fig. 5a shows u', v', $(g/N_B)T'/\overline{T}$ as functions of time at a fixed altitude for a possible event #1 GW that is downward and northwestward-propagating with $u'_H = 7\,\mathrm{m/s}$, $\lambda_H = 310$ km, $\tau_{Ir} = 2$ h and $\psi = 150°$, and Fig. 5b shows the corresponding hodograph in time. Here we use the GW polarization relations given by Eqs. (12)-(14) with $\gamma = 1.4$, $N_B = 0.02\,\mathrm{rad/s}$, $\mathcal{H} = 7$ km, $g = 9.8(R_\mathrm{E}/(R_\mathrm{E}+z))^2 = 9.6\,\mathrm{m/s^2}$, and $m > 0$ (because the GW is downward-propagating). We calculate ω_{Ir} from Eq. (3) using k and l from Eq. (20) and $\overline{U}$ and $\overline{V}$ from MERRA-2 at $z = 54$ km, and ensured that it equaled ω_{Ir} from Eq. (6). (Note that $\overline{U}$ and $\overline{V}$ from MERRA-2 are similar to the mean wind measured by the lidar at this altitude.) In Fig. 5a, u' and v' are approximately $\sim 180°$ out of phase because the GW propagates northward ($l > 0$) and westward ($k < 0$). Additionally, the T' peak precedes the u' peak by $\sim 90°$.

We employ the mid-frequency approximation for GWs whereby $N_B \gg \omega_{Ir} \gg f$, and assume that $|\lambda_z| \ll 4\pi\mathcal{H}$. Then Eqs. (13) and Eq. (14) become

$$\frac{T'}{\overline{T}} \simeq \frac{-im\omega_{Ir}}{gk}u'. \tag{24}$$

If a GW propagates downward and eastward, then $m > 0$ and $k > 0$ so that $T'/\overline{T} \propto -iu'$. Since x, y, and z are constants, $u' \propto u'_0 \exp(i\omega_r t)$ from Eq. (11), where u'_0 is the amplitude of u'. Then, $T'/\overline{T} \propto u'_0 \exp(i\omega_r(t - \pi/(2\omega_r))$, since $i = \exp(i\pi/2)$. Therefore T' peaks $90°$ after u' for a downward and eastward-propagating GW in this background wind. But if the GW propagates downward and westward, then $T'/\overline{T} \propto u'_0 \exp(i\omega_r(t + \pi/(2\omega_r))$ causing T' to peak $90°$ before u', as seen in Fig. 5a.

Fig. 5c-d shows the analogous results for a possible event #2 GW that propagates downward and northwestward with $\lambda_H = 1360$ km, $\tau_{Ir} = 7$ h, and $\psi = 110°$. As for the previous case, T' peaks $\sim 90°$ before u'. Note that the hodograph in Fig. 5d is rounder than in Fig. 5b because τ_{Ir} is larger.

While the hodograph of a monochromatic GW is a "perfect" ellipse (e.g., Fig. 5b,d), the hodographs of the lidar GWs are distorted ellipses due to contaminant GWs having similar τ_r and λ_z (see Fig. 3d-e,i-j). We now determine the best-fit intrinsic GW parameters, τ_{Ir}, λ_H and ψ, and corresponding 1-sigma errors from $u'(t)$, $v'(t)$, $T'(t)$ at a given altitude and location via searching parameter space for GWs consistent with the data and with the GW f-plane compressible dispersion and polarization relations for specified values of $\overline{U}$, $\overline{V}$, $\overline{T}$, γ, $\mathcal{H}$, N_B, g and f.

We perform 4 nested loops through specified ranges of values for λ_H, λ_z, τ_r and ψ. Here, λ_H ranges from $\lambda_H = 100$ to 3000 km and ψ ranges from $-180°$ to $180°$. Additionally, $|\lambda_z|$ ranges from $\overline{\lambda_z} - \sigma_{\lambda_z}$ to $\overline{\lambda_z} + \sigma_{\lambda_z}$ and $|\tau_r|$ ranges from $\overline{\tau_r} - \sigma_{\tau_r}$ to $\overline{\tau_r} + \sigma_{\tau_r}$ where $\overline{\lambda_z}$ and $\overline{\tau_r}$ are the best-fit values of λ_z and τ_r and σ_{λ_z} and σ_{τ_r} are the errors in these values from the PSD (see Table 1). In addition, τ_r ranges over negative and positive values, and $m = 2\pi/\lambda_z$ is negative (positive) for an upward (downward)-propagating GW. Within these loops, we set $\omega_r = 2\pi/\tau_r$ and $k_H = 2\pi/\lambda_H$, determine k and l from Eq. (20), and calculate ω_{Ir} from Eq. (3). We then calculate ω_{Ir} independently from Eq. (6) (or Eq. (9) if $|\lambda_z| \ll 4\pi\mathcal{H}$); if these ω_{Ir} values agree to within a small prescribed tolerance, we know this GW could have propagated in this atmosphere. We then check if the theoretical ratio of the maximum value of u' to the maximum value of v' (and/or the maximum values of $(g/N_B)T'/\overline{T}$ and w') from Eqs. (12)-(14) is within the specified tolerance range for the observed ratio of these

maximum values (e.g., from Fig. 3c,h). We calculate the former ratio by setting $u'(t)$ at a given altitude and location to be $u'(t) = u'_0 \exp(i\omega_r t)$, calculate $v'(t)$ from Eq. (12) then calculate $max(u')/max(v')$, where $max()$ denotes the maximum value. Several amplitude ratios can be used to better-constrain the resulting GW parameters if the contaminant GWs have relatively small amplitudes. We also calculate the phase of T' minus that of u', divide by $|\omega_r|$, and require this angle to be within a specified tolerance range from the observations. If the ratio(s) and phase shift(s) are within the specified tolerances, then this solution agrees with the observations and is saved as a viable solution.

Finally, we create histograms of the number of viable GW solutions as functions of λ_H, τ_{Ir}, c_H, c_{IH}, and ψ. Gaussian functions are then fitted to these histograms to obtain best-fit values with 1−sigma errors. Here, the intrinsic horizontal phase speed is

$$c_{IH} = \omega_{Ir}/k_H = c_H - U_H, \tag{25}$$

where $U_H = (k\overline{U} + l\overline{V})/k_H$. By definition, $c_{IH} \geq 0$ because the GW would have been absorbed by a critical level if it had reached zero from a positive value.

We now perform this analysis for events #1 and #2. From Fig. 3c,h, we estimate $u'_0/v'_0 = 1.5$ to 2.2 for event #1 and $u'_0/v'_0 = 0.5$ to 0.7 for event #2, where u'_0 (v'_0) is the amplitude of u' (v'). For both, we require T' to lead u' by 20° to 160° from Fig. 3c,h. We set $m > 0$ since these GWs are downward-propagating. We allow τ_r to range over positive and negative values to allow for the possibility that upward-propagating GWs have upgoing phase lines in time (see below). The background wind $(\overline{U}, \overline{V})$ and temperature $\overline{T}$ are obtained from MERRA-2 at ALOMAR on 13.25 January at $z = 54$ km and on 14.0 January at $z = 55$ km for events #1 and #2, respectively. In addition,

we set $\gamma = 1.4$, $\mathcal{H} = 7$ km, $g = 9.8(R_{\rm E}/(R_{\rm E}+z))^2$, $N_B = 0.02\,{\rm rad/s}$, $c_s = \sqrt{\gamma g \mathcal{H}}$, $f = 2\Omega \sin\theta$, $\Omega = 2\pi/(24{\rm h})$, and $\theta = 69.38°$.

Fig. 6 shows the number of (viable) GW solutions for events #1 and #2 as functions of λ_H, τ_{Ir}, c_H, c_{IH}, ψ, u_0'/v_0', $u_0'/[(g/N_B)T_0'/\overline{T}]$, $v_0'/[(g/N_B)T_0'/\overline{T}]$, and the angular phase shift between T' and u', where T_0' is the amplitude of T'. Both events contain medium to large-scale GWs, although the GWs in event #1 are mainly medium-scale, medium-frequency GWs with $\lambda_H = 250$ to 800 km and $\tau_{Ir} = 2-4$ h, while the GWs in event #2 are mainly large-scale, medium to low-frequency GWs with $\lambda_H = 800-1700$ km and $\tau_{Ir} = 6.5-8$ h. The GWs propagate northwestward during event #1, and northward during event #2. Note that the GWs in both events have $c_{IH} = 35-65\,{\rm m/s}$. We fit 1D Gaussian functions to these histograms. The best-fit parameters with 1-sigma errors are given in columns 4-8 in Table 1.

We now check that the upgoing phase lines (in time) below $z_{\rm knee}$ correspond to downward-propagating GWs. If an upward-propagating GW propagates against the background wind (i.e., $U_H < 0$), then its phase lines can be upgoing (not downgoing) in time in a $z-t$ plot if the GW is swept downstream in the same direction as the wind; this occurs if $c_H < 0$ (and $\tau_r < 0$) [see text surrounding Eq. (60) in *Vadas et al.*, 2018], which can only occur if $U_H < 0$ and $|U_H| > c_{IH}$ from Eq. (25). From Fig. 6c, $c_H > 0$ for all of the viable GW solutions. Therefore, the upgoing phase lines below $z_{\rm knee}$ correspond to downward-propagating GWs during both events. We conclude that events #1 and #2 were secondary GWs created from LBFs located southeast/south of ALOMAR at $z \sim 57$ and 64 km prior to 13.0 and 13.7 January, respectively.

4. Modeling the Primary and Higher-Order Gravity Waves over Europe on 12-14 January 2016

4.1. Description of the HIgh Altitude Mechanistic general Circulation Model with Specified Dynamics

The HIAMCM is a high-resolution, GW-resolving, global circulation model [*Becker and Vadas*, 2020, hereafter BV20]. It is based on a standard spectral dynamical core with a terrain-following hybrid vertical coordinate, and a correction for non-hydrostratic dynamics. Molecular viscosity, thermal diffusivity, and ion drag are included in the thermosphere so that a sponge layer is not needed or used there. The HIAMCM explicitly simulates momentum and energy deposition from GWs, including their spatial and temporal intermittency. This momentum and energy deposition occurs because resolved GW packets that become dynamically unstable are damped by the subgrid-scale turbulent diffusion (vertical and horizontal). Note that subgrid-scale diffusion is necessary for creating the wave-mean flow interactions, as is evident from the Wentzel-Kramers-Brillouin (WKB) solution for GWs damped by diffusion [e.g., *Lindzen*, 1981; *Becker*, 2012]. Further information is available in BV20.

In this study, we employ a model version similar to BV20, except we nudge the large-scale winds and temperatures from MERRA-2 reanalysis data (global down to $\lambda_H = 2000$ km) into the HIAMCM at $z = 0 - 70$ km in spectral space [B22]. The data used in this study is identical to that from B22. Because the MERRA-2 data is 3-hourly, we linearly-extrapolate the nudging for each model time step. We do not nudge scales having $\lambda_H < 2000$ km; hence, GWs are generated self-consistently in the HIAMCM (e.g., by wind flow over orography, imbalance of the polar night jet, etc.). The horizontal grid spacing is ~ 52 km, and the effective horizontal resolution corresponds to $\lambda_H = 156$ km.

The vertical grid spacing varies from $\sim$ 500 m below 70 km to $\sim$ 10 km at the highest altitudes, thereby allowing for the simulation of GWs with $\lambda_z \geq 1$ km below 70 km. GW perturbations with $\lambda_H \leq 2000$ km are extracted from the model output by interpolating the model data to constant height surfaces, then applying a spectral decomposition which only retains horizontal wavenumbers larger than 20 (corresponding to $\lambda_H \leq 2000$ km).

4.2. Modeled secondary gravity waves over ALOMAR, and comparison with lidar observations

Fig. 7a shows $T' \exp(-z/14\,\mathrm{km})$ as a function of time on 12-14 January 2016 at ALOMAR from the HIAMCM. Fig. 7b shows the same perturbations, but filtered (via Fourier transform) to retain GWs with $\tau_r \leq 11$ hr and $|\lambda_z| \geq 1$ km in order to remove the semi-diurnal and diurnal tides and to compare directly with the lidar observations. We see two GW fishbone structures with $z_{\mathrm{knee}} \sim 56 - 58$ km on January 13-13.6 and $z_{\mathrm{knee}} \sim 65 - 67$ km on January 13.7-14.3. Boundaries that enclose relatively "clean" structures are chosen as follows. Event #1 occurs at $45 < z < 68$ km on 12.9-13.7 January, and event #2 occurs at $40 < z < 85$ km on 13.7-14.3 January. Using the method described in Sec. 3.2, we estimate average knee altitudes of $z_{\mathrm{knee}} = 58$ and 66 km for events #1 and #2, respectively. The fishbone structures in Fig. 7b are contaminated with other GWs having upgoing and downgoing phases in time that appear to emanate from similar altitudes. As we show below, these are secondary GWs from neighboring LBFs which causes some of the GWs to have upgoing (downgoing) phase lines a few km above (below) the dashed line. (Appendix A shows how multiple body forces affect the fishbone structure.) Fig. 7c-d shows the GWs with upgoing and downgoing phases in time. Note that the GWs with

upgoing phases are mainly concentrated below the dashed lines, indicating that downward propagating GWs are generated in the region of the dashed line.

Fig. 8a shows a blow up of Fig. 7b. The GWs in the fishbone structures have $\tau_r \sim 4-9$ h and $|\lambda_z| \sim 10-25$ km. Fig. 8c shows the HIAMCM GWs with downgoing (upgoing) phases in time above (below) the dashed line in Fig. 7b. As for the lidar data, the hot-cold phases do not always line up because of constructive/destructive interference of the secondary GWs with contaminant GWs. We now compare the HIAMCM GWs with the ALOMAR lidar GWs. Fig. 8b shows $T' \exp(-z/14\,\text{km})$ for the ALOMAR lidar GWs from Fig. 1a. Remarkably, the amplitudes, location and times of the GWs are quite similar to the HIAMCM GWs in Fig. 8a during both events. Fig. 8d shows the ALOMAR lidar GWs with downgoing (upgoing) phases in time above (below) the dashed line in Fig. 2. The altitudes and parameters of the upward and downward-propagating secondary GWs are quite similar to the HIAMCM GWs from Fig. 8c. Note that the upward-propagating event #2 GWs are weaker in the HIAMCM than in the lidar data. This weakening may be due to the fact that the large-scale wind in the HIAMCM is only weakly nudged above 40 km and is not nudged above 70 km (see Fig. 1 in B22), and may therefore diverge from the actual atmospheric wind at these altitudes.

4.3. Comparison of the HIAMCM GWs with AIRS observations

We now compare the GWs in the HIAMCM with those extracted from the Atmospheric InfraRed Sounder (AIRS) data [*Hoffmann and Alexander*, 2009; *Gong et al.*, 2012; *Eckermann et al.*, 2019]. Temperature perturbations are retrieved from AIRS using a 4th order polynomial detrending zonally at each altitude, and are interpolated onto a 0.5° grid in latitude and longitude. The left column of Fig. 9 shows horizontal slices of T' from the HI-

AMCM at various altitudes of $z = 36 - 48$ km and at various times during 12-14 January. Medium-scale MWs with $\lambda_H \simeq 250$ km are seen around $\sim 40 - 50°$ N over the Alps and Carpathian Mountains at $z = 36 - 48$ km at $\sim 4 - 20°$ E and $\sim 25 - 35°$ E, respectively. Due to the orientation of the phase lines, these MWs mainly propagate zonally. In addition, high-latitude, larger-λ_H GWs are seen at $\sim -10°$ to $50°$ E and $\sim 50 - 70°$ N which propagate northwestward or southeastward. These high-latitude GWs are quite prevalent over Scandanavia, northern Europe, UK, and northwestern Russia. It was speculated by *Bossert et al.* [2020] that similar high-latitude GWs on 12 January 2016 were generated by the polar vortex; this hypothesis was confirmed for an event on 11 January 2016 [B22].

We apply an AIRS observational filter to the HIAMCM data. *Ern et al.* [2017] found that for medium-scale GWs with $\lambda_H \leq 600$ km and $\lambda_z \geq 24$ km, the sensitivity function is ≥ 0.8 [their Fig. S3 in Supporting Information]. Therefore, we remove HIAMCM GWs with $|\lambda_z| < 24$ km via Fourier filtering. The middle column of Fig. 9 shows the result. As expected, many of the GWs seen in the left column are absent here. The right column shows the AIRS T' at the same altitudes and times. In general, the parameters of the GWs (λ_H, orientation of the phase lines, location and amplitudes) in the observationally-filtered HIAMCM data agree very well with those in the AIRS data.

Fig. 9 provides an excellent validation of the horizontal structure of the GWs simulated by the HIAMCM at $z = 36 - 48$ km over Europe on 12-14 January 2016. In Appendix B we show that the HIAMCM GWs also compare well with those from AIRS over the Atlantic Ocean during this time period. The validation of the HIAMCM GWs with those from the ALOMAR lidar and AIRS provides the necessary justification to use this model to determine the source of the secondary GWs observed over ALOMAR.

4.4. X-Structure of the secondary GWs during event #1

Fig. 10a shows $T'\sqrt{\overline{\rho}/\rho_0}$ as a function of latitude and z at 15.7° E at 07 UT on 13 January from the HIAMCM. The colors are over-saturated to better-illuminate the secondary GWs. The upward and downward-propagating secondary GWs over ALOMAR at 69.2° N (turquoise line) are part of a faint secondary GW "X"-structure centered at $z = 55 - 60$ km and $58 - 62°$ N. These phase lines have a checkerboard appearance due to the constructive/destructive interference of the secondary GWs with other GWs. The dominant positive phase lines of the X-structure GWs are outlined with dashed lines, as we confirm in Fig. 11d. Importantly, primary GWs from below dissipate where the secondary GWs are generated, at $z \sim 50 - 55$ km at $55 - 62°$ N near the edge of the vortex (white line). The amplitudes of the secondary GWs are much smaller than those of the primary GWs, as is typical for secondary GWs generated by a LBF created by the breaking/dissipation of primary GWs [*Vadas et al.*, 2018]. Fig. 10b shows a blow-up of the primary GWs at 22 UT on 12 January, just prior to event #1. These primary GWs are part of a different X-structure centered at $z = 25 - 35$ km and $49 - 53°$ N (dash-dot lines). The upward primary GWs break/dissipate at $z \sim 50 - 55$ km and $55 - 62°$ N, which creates the LBF that generates the event #1 secondary GWs.

We now extract the X-structure of the secondary GWs. Fig. 11a is the same as Fig. 10a, but with different altitude ranges and color scales to emphasize the secondary GWs. Fig. 11b shows the northward/upward and southward/downward-propagating GWs from Fig. 11a. The primary GWs that dissipate at $z \sim 50 - 55$ km and at $55 - 62°$ N propagate upward/northward from $z \sim 25 - 35$ km and $\sim 50°$ N. Note that in the HIAMCM, wave damping is caused by the diffusion scheme. For the primary GWs in Fig. 11b, enhanced

diffusion coefficients are triggered by the amplitude growth and reduced static stability due to $d\overline{T}/dz < 0$ in the mesosphere (since $|\lambda_z|$ is virtually unchanged where the GWs dissipate).

Fig. 11c shows the southward/upward and northward/downward-propagating GWs obtained from Fig. 11a. Fig. 11d shows the extracted X-structure of the secondary GWs, which is obtained by retaining southward/upward and northward/downward propagating GWs for $z > z_{\rm knee}$ south of $\theta_{\rm cen}$ and for $z < z_{\rm knee}$ north of $\theta_{\rm cen}$, and by retaining northward/upward and southward/downward propagating GWs for $z > z_{\rm knee}$ north of $\theta_{\rm cen}$ and for $z < z_{\rm knee}$ south of $\theta_{\rm cen}$. Here, $z_{\rm knee} = 58$ km and $\theta_{\rm cen} = 60^\circ$ N. The dashed lines (which are the same as in Fig. 10a) overlay well with the X-structure of the secondary GWs. These secondary GWs have much smaller amplitudes than the primary GWs, as expected. Note that the upward/northward primary GWs contaminate the extracted X-structure of the secondary GWs (saturated colors in the lower left corner of Fig. 11d). Comparing Figs. 11b-c with Fig. 9, the GWs in the HIAMCM and in AIRS at $50-60^\circ$ N are mainly upward/northward primary GWs, because the downward/southward secondary GWs in this region have much smaller amplitudes.

4.5. Verification and parameters of the secondary GWs

We now verify that the HIAMCM fishbone structure GWs in Fig. 8 are secondary GWs (i.e., that they have the same parameters and propagation directions above and below $z_{\rm knee}$). We transform T' onto a 2D Cartesian grid that is perpendicular to a line from the center of Earth to its surface at 24.7° E and 53.2° N [*Vadas and Becker*, 2018, their Appendix B]. The coordinates on this 2D plane are (x'', y''). Fig. 12a-b shows horizontal slices of T' for GWs with $450 < \lambda_H < 2000$ km at $z = 54$ km (below $z_{\rm knee}$) and at $z = 62$

591 km (above $z_{\rm knee}$) at 2 UT on 13 January during event #1. GWs with $\lambda_H \sim 500-1500$ km
592 are seen above and below $z_{\rm knee}$ near ALOMAR (asterisk). The orientation of their phase
593 lines indicate that they propagate northwest or southeastward. These are the secondary
594 GWs in the fishbone structure. We draw a line perpendicular to these phase fronts that
595 passes through ALOMAR, and place a triangle at $\theta_{\rm cen} = 60^\circ$ N in Fig. 12a-b. This
596 triangle is the estimated location of the LBF which generated these event #1 GWs. Since
597 secondary GWs generated by a LBF primarily radiate upward and downward, in and
598 against the direction of the LBF, they constitute 4 distinct "headlights" of GWs (if the
599 background wind is negligible) [*Vadas et al.*, 2003]. Therefore, the northwestward or
600 southeastward propagation directions of the secondary GWs is consistent with either a
601 northwestward or a southeastward LBF.

602 Fig. 12d-e show keograms of T' as functions of x'' below and above $z_{\rm knee}$ at $y'' = 1500$
603 km, and Fig. 12g-h show keograms as functions of y'' below and above $z_{\rm knee}$ at $x'' = -500$
604 km. This location, $(x'', y'') = (-500, 1500)$ km, is somewhat south of ALOMAR. The GWs
605 propagate northwestward over ALOMAR during event #1 (dashed lines), with similar x''
606 and y'' phase speeds below and above $z_{\rm knee}$ of $c_x \sim -40.5$ m/s and $c_y \sim 23.1$ m/s. Here,
607 $c_x = \omega_r/k = \lambda_x/\tau_r$ and $c_y = \omega_r/l = \lambda_y/\tau_r$ are the phase speeds in the x" and y'' directions,
608 respectively. From Eq. (20),

$$\tan\psi = l/k = c_x/c_y. \tag{26}$$

609 Therefore, the estimated propagation direction of these GWs is $\psi \sim 150^\circ$ (counter-
610 clockwise from east). The horizontal phase speed of a GW is [e.g., Eqs. (13)-(14) of

Vadas and Becker, 2018]

$$c_H = \frac{\omega_r}{k_H} = \frac{1}{\sqrt{(k/\omega_r)^2 + (l/\omega_r)^2}} = \frac{1}{\sqrt{1/c_x^2 + 1/c_y^2}}. \quad (27)$$

Therefore, $c_H \sim 20\,\mathrm{m/s}$. From Fig. 12d-e and Fig. 12g-h, $\tau_r \sim 8$ h above and below $z_{\rm knee}$, which yields $\lambda_H = c_H/\tau_r \sim 580$ km. These event#1 parameters, $\lambda_H \sim 580$ km, $\tau_r \sim 8$ h, $c_H \sim 20\,\mathrm{m/s}$, and $\psi \sim 150°$, agree very well with the values deduced from the lidar observations (see Table 1). Therefore, we conclude that the HIAMCM is able to simulate the event #1 GWs very well. Because the GW parameters are similar above and below $z_{\rm knee}$, we conclude that the event #1 GWs are secondary GWs, and that they are created by a northwestward or a southeastward LBF that is located southeast of ALOMAR at $\sim 35°$E and $\sim 60°$N. The turquoise arrow in Fig. 12a-b shows the approximate propagation direction of the secondary GWs.

Fig. 12c shows a horizontal slice of T' at 22 UT on 13 January for the event #2 GWs with $450 < \lambda_H < 2000$ km at $z = 71$ km. The map has a disorganized checkerboard appearance, which occurs when there is significant constructive/destructive interference between multiple wave packets. There is a small wave packet south of ALOMAR with $\lambda_H \sim 800 - 1000$ km. Corresponding keograms as functions of x'' and y'' are shown in Fig. 12f,i above $z_{\rm knee}$. Although it is difficult to locate this packet in the noisy keograms, the event #2 GWs may propagate northward with $c_x \sim -2.67\,\mathrm{m/s}$ and $c_y \sim 31.8\,\mathrm{m/s}$ (dashed-dotted lines), which yield $\psi \sim 95°$ and $c_H \sim 2.7\,\mathrm{m/s}$. Although ψ and λ_H agree well with the values in Table 1, c_H is too small. This discrepancy is likely due to the difficulty of locating the GW packet without additional filtering, which is beyond the scope of this paper. For the rest of this paper, we focus on the event #1 GWs.

4.6. Parameters of the primary GWs that created event #1

We now determine the parameters of the primary GWs that created event #1. Fig. 13a-b show horizontal slices of T' for GWs with $200 < \lambda_H < 400$ km at 22 UT on 12 January at $z = 45$ and 55 km. A GW packet with $\lambda_H \sim 400$ km propagates northwest or southeastward at the approximate location of the LBF (triangle). This packet is not seen northwest of the LBF because the primary GWs break and dissipate there, near the edge of the polar vortex (white line). Note that the lines of constant phase are roughly parallel to the edge of the polar vortex. Fig. 13c and d shows keograms of the primary GWs just southeast of the LBF (turquoise lines). These GWs propagate slowly southeastward on 12 January and slowly northwestward on 13-13.5 January. We estimate $\psi \sim -60°$ and $c_H \sim 1.2\,\mathrm{m/s}$ on 12.0-13.0 January, and $\psi \sim 148°$ and $c_H \sim 5.5\,\mathrm{m/s}$ on $13.0 - 13.5$ January. If the GWs on 12 January dissipate, a southeastward LBF is created with $\psi \sim -60°$, which would excite southeastward and northwestward propagating secondary GWs. Therefore, the propagation direction of this primary GW is consistent with the propagation direction of the observed event #1 secondary GWs (i.e., $\psi = 150°$).

Fig. 13e and f show keograms of the northern edge of the MWs generated by the Alps. The MWs propagate very slowly, and do not propagate north of $y'' = 0$ (i.e., 53° N) on 12 January. Therefore, these MWs could not have created the event #1 LBF.

4.7. Source of the primary GWs that created event #1

Fig. 14a shows a global view of T' at 22 UT on 12 January at $z = 20$ km. MWs are seen over Europe and Greenland, and high-latitude GWs are seen over northern Europe and Siberia. We also see GWs in the jet exit region in the lower stratosphere east of Newfoundland over the western Atlantic Ocean. Fig. 14b shows T' at $z = 42$ km.

The high-latitude GWs over Norway, Sweden, northern Scotland and west of Ireland are aligned with the streamfunction and are located near the edge of the polar vortex.

Fig. 15 shows horizontal slices of T' from $z = 15$ to 70 km at 2 UT on 13 January. At $z = 15$ and 20 km, MWs are present south of 50° N (e.g., over the Alps). Their phase lines are roughly perpendicular to the background wind, as indicated by the streamfunction. At $z = 26$ km, high-latitude GWs appear north of 50° N. These GWs are separated latitudinally from the MWs to the south, and are also observed north and east of the Alps over Norway and Scotland. At $z = 42$ km, the phase lines of the high-latitude GWs and the MWs appear to blend together at $52 - 55°$ N, thereby incorrectly implying that these high-latitude GWs (near the LBF) might be trailing MWs [*Dörnbrack*, 2021]. These high-latitude GWs also occur over Norway and Scotland, thereby countering the idea that these high-latitude GWs are trailing MWs. At $z = 53$ km, the high-latitude GWs and MWs are dissipating, as indicated by the relatively weak increase in their amplitudes from $z = 42$ km to 53 km (since the amplitude of a non-dissipating GW would have increased by $\exp(\Delta z/2\mathcal{H}) = \exp(11/14) = 2.2$ in an isothermal, constant wind atmosphere). At $z = 70$ km, the high-latitude GWs and MWs have dissipated.

Fig. 16 shows longitude-height slices of $T'\sqrt{\overline{\rho}/\rho_0}$ at 22 UT on 12 January. At 45° N, MWs occur over the Alps and Carpathian Mountains. At 51° N, the MWs are mostly absent. Instead, GWs within X-structures are generated at $z \sim 25 - 35$ km at $10 - 50°$ E. X-structure GWs are also generated at $z \sim 25 - 35$ km at 59° N, although the generation region is further east. At 69° N, GW generation is small.

Fig. 17 shows latitude-height slices of $T'\sqrt{\overline{\rho}/\rho_0}$ at 22 UT on 12 January. GWs within X-structures are generated at $z \sim 25 - 45$ km and $50 - 60°$ N for 40° W to 50° E, including

at 25° W and 40° W over the Atlantic Ocean. The generation regions are close to the edge of the stratospheric polar vortex, $\sim 5-10$ km below the wind maximum where the vertical wind shear is large. Note that there is minimal GW generation near the edge of the polar vortex at 100° E because the vortex is weak there, although MWs are generated over the Plateau of Tibet at $\sim 40°$ N. Therefore, we conjecture that the X-structure GWs at $40-50°$ E are generated by imbalance of the stratospheric polar night jet; we verify this conjecture in Sec. 4.8. In general, the X-structure GWs dissipate at $z \sim 50-65$ km, which is a few to ~ 20 km above the altitude where the wind speed in the polar night jet is maximum.

4.8. MKS and MPC formalism: Primary and secondary GWs from the polar vortex

B22 derived the mesoscale kinetic energy source (MKS), which describes the rate at which GWs extract kinetic energy from the geostrophic flow. They found that the MKS is positive in regions where GWs are generated or amplified, which can occur when GWs are generated by an imbalance of the polar night jet, or when GWs from another source propagate from below into a shear region. They also derived the mesoscale potential energy flux convergence (MPC), which is a 3D generalization (in spherical geometry) of the usual vertical potential energy flux convergence. This energy flux convergence is the main contributor to the energy deposition of GWs in the single column picture [e.g., *Becker*, 2017]. B22 found that GWs are generated by imbalance of the stratospheric polar night jet, and that these GWs are amplified by the jet in regions where MKS>0 and MPC<0, as long as the region is free of dissipating GWs that propagated upward

from below. In the case of energy deposition by dissipating GWs from below, MKS<0 and MPC>0.

Fig. 18a-b shows the MKS and MPC in the stratosphere averaged from $z = 30-50$ km and 21-24 UT on 12 January. South of 50° N, MWs are partly reamplified by the polar night jet. The alternating pattern of MPC south of $\sim 50°$ N is indicative of individual MW packets with finite horizontal extent, thereby causing minus/plus-patterns of horizontal potential energy flux convergence in the direction these waves propagate intrinsically (i.e., westward). The reamplification of the MWs extends as far north as $\sim 52°$ N at $0-20°$ E. North of 50°, primary high-latitude GWs are generated by the polar night jet where MKS>0 and MPC<0; this occurs over a broad region at $20-40°$ E and $50-55°$ N.

The generation region for the high-latitude GWs can also be seen in Fig. 19c-d, which shows the density-weighted MKS and MPC averaged at $52-60°$ N and 21-24 UT. This generation region occurs at $z = 25-50$ km at $15-50°$ E. We also show the mesoscale vertical potential energy flux density (PEFD) in Fig. 19, which is positive (negative) for upward (downward)-propagating GWs [e.g., BV18]. The PEFD in Fig. 19c-d is positive at $z = 25-50$ km at $10-50°$ E, and increases from 0.1 to $0.5-0.7$ at $z = 20-45$ km at $15-50°$ E. This behavior confirms that the high-latitude GWs are generated at $z > 20$ km. Above $z \sim 50$ km, however, MKS<0, MPC>0 and the PEFD decreases in altitude, thereby indicating that these high-latitude GWs are dissipating and are depositing momentum and energy into the atmosphere. Importantly, there is a small GW generation region at $z \sim 58-60$ km and $32-38°$ E where MKS>0 and MPC<0 in Fig. 19c-d; this generation region is co-located with the event #1 LBF (labeled "B").

Fig. 18c-d shows the MKS and MPC in the lower mesosphere averaged from $z = 55-60$ km and 21-24 on 12 January. Negative MKS and positive MPC over the Alps and Carpathian Mountains indicate strong MW dissipation. North of 52° N, GW generation occurs over southern Sweden and at $32-38°$ E and $54-60°$ N. This latter region overlaps with the event #1 LBF ("B"). We also show in Fig. 18c-d the horizontal body forces vectors at $z = 57$ km and 57.75°N at 24, 30, and 36°E averaged from 22-23 UT. The forces at these locations are southeastward with average amplitudes of $\sim 150-250$ m/s/day. Thus the primary GWs created by the polar vortex were propagating southeastward when they dissipated, which agrees with the keograms in Figs. 13c,d.

Fig. 20a-b shows the zonal and meridional components of the GW drag (GWD) averaged over $z = 30-50$ km and 22-23 UT on 12 January. South of 50° N, dissipating MWs create a westward drag with a weak northward component. North of 50°, however, the drag is southward with a weak eastward component. Fig. 20c-d shows the zonal and meridional components of the GWD averaged from $z = 55-60$ km and 22-23 UT. The drag is southeastward at $20-40°$ E and $55-60°$ N (see Figs. 18c,d and 19c-d), which agrees well with the location of the event # 1 LBF ("B").

We thus conclude that the primary high-latitude GWs which led to event #1 were created and amplified by the polar night jet. Upon dissipation, they created multiple southeastward LBFs at $20-40°$ E and $55-60°$ N, one of which excited the event #1 secondary GWs observed over ALOMAR.

4.9. MKS and MPC formalism: Mountain waves at mid-latitudes

Fig. 19a shows the density weighted MKS averaged from $44-50°$ N and 21-24 UT on 12 January. MW signatures are seen at $0-15°$ E (Alps), $23-32°$ E (Carpathian Mountains)

and $36-50^\circ$ E (Caucasus Mountains). The positive to negative MPC seen for each MW signal in Fig. 19b results as follows. There is a westward potential energy flux upstream of the mountainous region because the intrinsic group velocity of the MWs is predominantly westward, which causes the energy flux to emerge eastward of the mountain range and to converge further westward. These MWs dissipate at $z \sim 40-50$ km. Additionally, there is a region of negative PEFD at $5-15^\circ$ E farther to the north in Fig. 19c-d, which indicates downward-propagating GWs. These are likely downward-propagating secondary GWs from MW breaking.

5. Conclusions

In this paper, we analyzed the GWs within two fishbone structures observed by a Rayleigh lidar in the stratosphere and lower mesosphere above ALOMAR in northern Norway during 12-14 January 2016. These structures were located at $z \sim 40-85$ km on $\sim 13.1-13.6$ January and $13.7-14.2$ January with $z_{\rm knee} = 57$ and 64 km, respectively. Because the hodographs were significantly distorted due to contamination from secondary GWs from neighboring LBFs, we introduced an alternative method to extract the predominant GW parameters from the data. This method involves solving the GW polarization and dispersion relations for the observed vertical wavelengths and wave periods, and constraining the results with the observed amplitude ratios and phase shifts. We found that the event #1 GWs propagated northwestward, were medium-scale and medium-frequency, and had $\psi = (135 \pm 8)^\circ$, $\lambda_H = 477 \pm 280$ km, $\tau_{Ir} = 2.8 \pm 0.9$ h, $\tau_r = 6.7 \pm 1.7$ h, $c_H = 20.0 \pm 9.5$ m/s, and $c_{IH} = 48.2 \pm 9.4$ m/s. We found that the event #2 GWs propagated northward, were large-scale inertia GWs, and had $\psi = (91 \pm 8)^\circ$, $\lambda_H = 1472 \pm 228$ km, $\tau_{Ir} = 7.6 \pm 0.6$ h, $\tau_r = 8.3 \pm 2.0$ h, $c_H = 57.9 \pm 16.6$ m/s, and

$c_{IH} = 52.1 \pm 10.3\,\mathrm{m/s}$. Because the GW parameters and propagation directions were similar above and below z_{knee}, and because we found that the GWs with upgoing phases in time below z_{knee} were downward-propagating, we concluded that these GWs were secondary GWs created by local body forces (LBFs) southeast and south of ALOMAR at $z = 57$ and 64 km, respectively.

To determine the source of the primary GWs which created the LBFs, we modeled these events using the high-resolution, GW-resolving HIAMCM with the large-scale wind and temperature nudged to MERRA-2 reanalysis in spectral space. Remarkably, we found that the HIAMCM simulated similar fishbone structures at similar times and altitudes, with $z_{\mathrm{knee}} = 58$ and 66 km for events #1 and #2, respectively. To further validate the model, we compared the HIAMCM GWs with those observed by the AIRS satellite over Europe and the Atlantic Ocean during these events, and found that they agreed quite well. This agreement justified our use of the HIAMCM to determine the cause of the observed events over ALOMAR.

We found that the event #1 GWs (modeled by the HIAMCM) were part of an "X" structure in latitude and altitude at 15.7° E, with a center at $z = 58$ km and 60° N. Using keograms, we found that the GW parameters and propagation directions above and below z_{knee} were nearly the same. Therefore, we concluded that these GWs were secondary GWs created by a LBF, and that the LBF was located at $z = 58$ km, 35° E and 60° N. We found that these secondary GWs had $\lambda_H \sim 580$ km, $\tau_r \sim 8$ h, $c_H \sim 20\,\mathrm{m/s}$, and $\psi \sim 150°$, which agreed very well with the values deduced from the lidar observations.

We then investigated the wave dynamics which led to the event #1 LBF. We found that primary GWs propagated upward from below and dissipated at $z \sim 50 - 55$ km and

785 $55-62^\circ$ N, thereby creating this LBF. These primary GWs were part of a different X-
786 structure generated/amplified at $z \sim 25-35$ km at $49-53^\circ$ N. Because this source region
787 was located near the edge of the polar vortex where the vertical wind shear was large
788 (below the altitude of the wind maximum), and because this region was separate from the
789 MWs at midlatitudes, we postulated that these GWs were created by the imbalance of the
790 stratospheric polar night jet and were amplified by the jet in regions where the vertical
791 wind shear was large. To test this conjecture, we examined the mesoscale kinetic energy
792 source (MKS), which describes the rate at which GWs extract kinetic energy from the
793 geostrophic mean flow, as well as the mesoscale potential energy flux convergence (MPC),
794 because GWs are amplified by the jet in regions where the vertical wind shear is large
795 such that MKS>0 and MPC<0. We found that north of $\sim 50^\circ$ N at $15-50^\circ$ E, primary
796 GWs were generated at $z = 25-50$ km by the polar night jet, and then dissipated above
797 $z \sim 50$ km. We also found a small GW generation region above this dissipation region
798 at $z \sim 58-60$ km and $30-40^\circ$ E which contained LBFs (including the event #1 LBF).
799 We therefore concluded that these LBFs generated the secondary inertia GWs observed
800 over ALOMAR, and that these LBFs were generated by the breaking and dissipation of
801 primary GWs. In turn, these primary GWs were generated by the imbalance of the polar
802 night jet and were amplified by the vertical wind shear in the jet below the wind maximum
803 near the vortex edge.

804 Because the secondary GWs in events #1 and 2 have relatively small horizontal phase
805 speeds, they are not expected to survive the large background winds in the mesosphere-
806 lower-thermosphere (MLT) region and propagate into the thermosphere. Indeed, the
807 secondary GWs observed over ALOMAR are seen to dissipate at $z \sim 65-70$ km ($z \sim 70-$

808 80km) during events #1 (#2) (see middle column of Fig. 2). These GWs likely undergo
809 wave breaking, since λ_z does not decrease significantly during dissipation. These processes
810 likely generate tertiary GWs. A companion paper explores these higher-order GWs to
811 $z \sim 400$ km on 12-14 January by analyzing the HIAMCM data and comparing with data.
812 That study will enable a more-complete and accurate picture of how momentum and
813 energy are transferred via multi-step vertical coupling from the polar vortex and other
814 lower atmosphere sources into GWs and variability in the rarefied thermosphere.

6. Open Research

815 MERRA-2 reanalysis data was used to nudge the HIAMCM, and is available in English
816 for download at https : //gmao.gsfc.nasa.gov/reanalysis/MERRA-2/data_access/. The
817 model data shown in this paper will be available at time of publication in English at
818 https://www.cora.nwra.com/vadas/Vadas-etal-JGR-2022-SecGWs-files/.

819 **Acknowledgments.**

820 We would like to thank Dr. Xinzhao Chu and 2 anonymous reviewers for helpful com-
821 ments. SLV was supported by NSF Grants # 1822867 and # 1832988. SLV and EB were
822 supported by DARPA contract 140D6319C0032, and NASA grants 80NSSC20K0628 and
823 80NSSC19K0836. The model data shown in this paper will be available via NWRA's web-
824 site at https://www.cora.nwra.com/vadas/Vadas_etal_January2016-JGR_2022_files/ once
825 this paper is published. EB was additionally supported by the Leibniz Institute of At-
826 mospheric Physics at the University of Rostock (IAP), which provided the HPC facility
827 used for this study. KB was supported by NSF grant AGS-2052993 and NASA grant
828 80NSSC19K0836. GB acknowledges the contribution of the project W1 (Gravity wave

parameterisations for the atmosphere) of the Collaborative Research Centre TRR 181 "Energy Transfers in Atmosphere and Ocean" funded by the Deutsche Forschungsgemeinschaft (DFG, German Research Foundation) under project number 274762653. LH acknowledges the Juehlich Supercomputing Centre for providing computing time on the JUWELS cluster to process the AIRS high-resolution temperature retrievals. VLH acknowledges NASA grant 80NSSC19K0834. The views, opinions and/or findings expressed are those of the author and should not be interpreted as representing the official views or policies of the Department of Defense or the U.S. Government.

Appendix A: Secondary Gravity Waves Excited by Local Body Forces

In Sec. 4.6, we found that although the primary GW packet which created event #1 was fairly coherent near its breaking level, its amplitude and propagation direction varied somewhat at $50-60^\circ$ N (see Fig. 13a-b), thereby resulting in body force vectors having different amplitudes and directions (black arrows in Fig. 20c-d). Therefore, instead of a single large LBF being created where the primary GW packet broke, many neighboring LBFs having different amplitudes and directions at somewhat different altitudes, locations and times were created. Previous studies found that many adjacent LBFs are common in the wintertime stratosphere and mesosphere in regions of GW breaking [*Vadas and Becker*, 2018, their Figs. 21-22], [*Vadas and Becker*, 2019, their Figs. 8-9].

In this appendix, we model the secondary GWs excited by multiple idealized neighboring LBFs. We solve the linear, f-plane compressible fluid equations for an idealized Gaussian LBF that begins at 12.7 January, is located at 35° E, 60°N and $z_{\rm knee}$ = 57 km, and has a full width of $\mathcal{D}_H = 4.5\sigma_x = 4.5\sigma_y$ = 500 km, a full depth of $\mathcal{D}_z = 4.5\sigma_z$ = 12 km, a full duration of χ = 2.6 h, and a direction of $\psi = 315^\circ$. We assume that the

background atmosphere has $\overline{T} = T_0 = 231$ K, $N_B = 0.02\,\mathrm{rad/s}$ and $\overline{\rho} = \overline{\rho}_0 \exp(-z/\mathcal{H})$ with $\mathcal{H} = 6.9$ km. The total horizontal force is $\mathbf{F}\mathcal{F}$ [RHS of Eq.(1) in *Vadas*, 2013], where $\mathbf{F}$ depends on space and $\mathcal{F}$ depends on time. The solutions were calculated in that work for $\mathcal{F} = [1 - \cos(2\pi n t/\chi)]/\chi$ for $0 \le t \le \chi$ and $\mathcal{F} = 0$ otherwise, where n is an integer [Eq.38 of *Vadas*, 2013]. Here we choose $n = 1$, and assume a Gaussian for the LBF of

$$\mathbf{F} \;=\; F_x\hat{\mathbf{i}} + F_y\hat{\mathbf{j}} = A(\cos\psi\hat{\mathbf{i}} + \sin\psi\hat{\mathbf{j}}) \exp\left[-\frac{(x-x_0)^2}{2\sigma_x^2} - \frac{(y-y_0)^2}{2\sigma_y^2} - \frac{(z-z_0)^2}{2\sigma_z^2}\right]. \qquad \text{(A1)}$$

Here A is the amplitude of $\mathbf{F}$ (in m/s), and the center of the force is at (x_0, y_0, z_0). We choose (x_0, y_0) to be the estimated event #1 LBF location of 35° E and 60°N, and evaluate the solutions at ALOMAR (i.e., at $x = -888$ km and $y = 1000$ km in this coordinate system). In order that the secondary GWs have similar amplitudes as those observed by the lidar (i.e., Fig. 8), we choose $A = 2000$m/s, which yields an average acceleration in the vicinity of the LBF of $A/(4\chi) \sim 0.053\,\mathrm{m/s^2}$ or $\sim 192\,\mathrm{m/s/h}$. This acceleration is significantly larger than the average accelerations there (black arrows in Fig. 20c-d).

Fig. 21a shows $T' \exp(-z/14\,\mathrm{km})$ as a function of altitude and time at the location of ALOMAR for a single LBF. A fishbone structure is apparent, which contains upward and downward-propagating secondary GWs. Fig. 21b shows the corresponding result for two neighboring LBFs; the first LBF is the same as in Fig. 21a, while a second LBF has the same amplitude, but occurs 1 h earlier, and is 500 km west, 200 km north, and 4 km higher than the first LBF. Although the main fishbone structure is still apparent, a weak checkerboard appearance occurs from constructive/destructive interference of the secondary GWs from both LBFs. This appearance makes it more difficult to determine z_{knee} and to identify the GW parameters from the corresponding hodographs.

Appendix B: Comparison of HIAMCM GWs with AIRS GWs over the Atlantic Ocean

In order to further validate the HIAMCM, we compare the GWs in the HIAMCM with those from AIRS over the Atlantic Ocean during this time period. The left column in Fig. 22 shows T' for the HIAMCM GWs at $z = 36$ km and at various times from 15 UT on 12 January to 3 UT on 14 January. MWs over southern Greenland and GWs generated by the polar vortex with phase lines aligned with the streamfunction (grey lines in left column) are seen. Additionally, GWs generated by the imbalance of the tropospheric jet in the jet exit region east of Newfoundland are seen. This latter source occurs where the streamfunction at $z = 12$ km expands (grey lines in middle column).

The middle column of Fig. 22 shows the observationally-filtered HIAMCM T' for GWs with $|\lambda_z| \geq 24$ km. In general, the large-λ_z MWs and GWs from the polar vortex have small amplitudes. For the MWs over Greenland, this is likely because the polar night jet is displaced south of Greenland (see Fig. 4a), which limits the growth of $|\lambda_z|$. For the GWs excited by the polar vortex, this is likely because 1) the wind in the polar vortex is weaker over the Atlantic Ocean than over northern Europe, thereby limiting the growth of $|\lambda_z|$, and 2) the vertical wind shear is smaller over the Atlantic Ocean, which limits the amplification of the polar vortex-generated GWs (see Fig. 17a-b). The right column of Fig. 22 shows the AIRS T'. In general, very good agreement is seen between the observationally-filtered HIAMCM GWs and the AIRS GWs.

References

Alexander, M. J., and H. Teitelbaum (2007), Observation and analysis of a large amplitude mountain wave event over the antarctic peninsula, *J. Geophys. Res.*, *112*, D21,103, doi: 10.1029/2006JD008368.

Alexander, M. J., and H. Teitelbaum (2011), Three-dimensional properties of andes mountain waves observed by satellite: A case study, *J. Geophys. Res.*, *116*, D23,110, doi: 10.1029/2011JD016151.

Alexander, M. J., J. R. Holton, and D. R. Durran (1995), The gravity wave response above deep convection in a squall line simulation, *J. Atmos. Sci.*, *52(12)*, 2212–2226, doi:10.1175/1520-0469.

Alexander, S., A. Klekociuk, and D. Murphy (2011), Rayleigh lidar observations of gravity wave activity in the winter upper stratosphere and lower mesosphere above davis, *J. Geophys. Res.*, *116 (D13109)*, doi:10.1029/2010JD015164.

Banks, P., and G. Kockarts (1973b), *Aeronomy Part B*, Academic Press, New York, 355 pp.

Baumgarten, G. (2010), Doppler Rayleigh/Mie/Raman lidar for wind and temperature measurements in the middle atmosphere up to 80 km, *Atmos. Meas. Tech.*, *3*(6), 15091518, doi:10.5194/amt-3-1509-2010.

Baumgarten, G., J. Fiedler, J. Hildebrand, and F.-J. Lübken (2015), Inertia gravity wave in the stratosphere and mesosphere observed by Doppler wind and temperature lidar, *Geophys. Res. Lett.*, *42*, 10,92910,936, doi:10.1002/2015GL066991.

Becker, E. (2012), Dynamical control of the middle atmosphere, *Space Sci. Rev.*, *168*, 283–314, doi:10.1007/s11214-011-9841-5.

Becker, E. (2017), Mean-flow effects of thermal tides in the mesosphere and lower thermosphere, *J. Atmos. Sci.*, *74*, 2043–2063, doi:10.1175/JAS-D-16-0194.1.

Becker, E., and S. L. Vadas (2018), Secondary gravity waves in the winter mesosphere: Results from a high-resolution global circulation model, *J. Geophys. Res. Atmos.*, *123*, doi:10.1002/2017JD027460.

Becker, E., and S. L. Vadas (2020), Explicit global simulation of gravity waves in the thermosphere, *J. Geophys. Res. Space Physics*, doi:10.1029/2020JA028034.

Becker, E., S. L. Vadas, K. Bossert, V. L. Harvey, C. Zülicke, and L. Hoffmann (2022), A high-resolution whole-atmosphere model with resolved gravity waves and specified large-scale dynamics in the troposphere and stratosphere, *J. Geophys. Res. Space Physics*, *127*, e2021JD035,018, doi:10.1029/2021JD035018.

Beres, J. H., M. J. Alexander, and J. R. Holton (2002), Effects of tropospheric wind shear on the spectrum of convectively generated gravity waves, *J. Atmos. Sci.*, *59*, 1805–1824.

Bossert, K., S. L. Vadas, L. Hoffmann, E. Becker, V. L. Harvey, and M. Bramberger (2020), Observations of stratospheric gravity waves over Europe on 12 january 2016: The role of the polar night jet during the DEEPWAVE campaign, *J. Geophys. Res. Atmos.*, *125*, doi:10.1029/2020JD032893.

Chen, C., and X. Chu (2017), Two-dimensional Morlet wavelet transform and its application to wave recognition methodology of automatically extracting two-dimensional wave packets from lidar observations in Antarctica, *J. Atmos. Sol.-Terr. Phys.*, doi:10.1016/j.jastp.2016.10.016.

Chen, C., X. Chu, A. J. McDonald, S. L. Vadas, Z. Yu, W. Fong, and X. Lu (2013), Inertia-gravity waves in antarctica: A case study using simultaneous lidar and radar

measurements at McMurdo/Scott Base (77.8°S, 166.7°E), *J. Geophys. Res.*, *118*, doi: 10.1002/jgrd.50318.

Chen, C., X. Chu, J. Zhao, B. R. Roberts, Z. Yu, W. Fong, X. Lu, and J. A. Smith (2016), Lidar observations of persistent gravity waves with periods of 3−10 h in the Antarctic middle and upper atmosphere at McMurdo (77.83°S, 166.67°E), *J. Geophys. Res. Space Physics*, *121*, 1483–1502, doi:10.1002/2015JA022127.

Chun, H.-Y., and Y.-H. Kim (2008), Secondary waves generated by breaking of convective gravity waves in the mesosphere and their influence in the wave momentum flux, *J. Geophys. Res.*, *113*, D23,107, doi:10.1029/2008JD009792.

Cot, C., and J. Barat (1986), Wave-turbulence interaction in the stratosphere: A case study, *J. Geophys. Res.-Atmos.*, *91*, 2749–2756.

Dörnbrack, A. (2021), Stratospheric mountain waves trailing across Northern Europe, *J. Atmos. Sci.*, *78*, 2835–2857, doi:10.1175/JAS-D-20-0312.1.

Dörnbrack, A., S. Gisinger, N. Kaifler, T. C. Portele, M. R. M. Bramberger, M. Gerding, M. Söder, N. Zagar, and D. Jelic (2018), Gravity waves excited during a minor sudden stratospheric warming, *Atmos. Chem. Phys.*, *18*, 12,915–12,931, doi:10.5194/acp-18-12915-2018.

Eckermann, S. D., J. D. Doyle, P. A. Reinecke, C. A. Reynolds, R. B. Smith, D. C. Fritts, and A. dreas Drnbrack (2019), Stratospheric gravity wave products from satellite infrared nadir radiances in the planning, execution, and validation of aircraft measurements during deepwave, *Journal of Applied Meteorology and Climatology*, *58*, 2049–2075, doi:10.1175/JAMC-D-19-0015.1.

957 Ern, M., L. Hoffmann, and P. Preusse (2017), Directional gravity wave momentum fluxes
958 in the stratosphere derived from high-resolution airs temperature data, *Geophys. Res.*
959 *Lett.*, *44*, 475–485, doi:10.1002/2016GL072007.
960 Fiedler, J., G. Baumgarten, B. Uwe, P. Hoffmann, N. Kaifler, and F.-J. Lübken (2011),
961 Nlc and the background atmosphere above alomar, *Atmospheric Chemistry and Physics*
962 *Discussions*, *11*, doi:10.5194/acp-11-5701-2011.
963 Fovell, R., D. Durran, and J. Holton (1992), Numerical simulation of convectively gener-
964 ated gravity waves, *J. Atmos. Sci.*, *49*, 1427–1442.
965 Fritts, D., and Z. Luo (1992), Gravity wave excitation by geostrophic adjustment of the
966 jet stream, part 1: Two-dimensional forcing, *J. Atmos. Sci.*, *49*, 681–697.
967 Fritts, D., R. Smith, M. Taylor, J. Doyle, S. Eckermann, A. Drnbrack, M. Rapp,
968 B. Williams, P. Pautet, K. Bossert, N. Criddle, C. Reynolds, P. Reinecke, M. Uddstrom,
969 M. Revell, R. Turner, B. Kaifler, J. Wagner, T. Mixa, C. Kruse, A. Nugent, C. Watson,
970 S. Gisinger, S. Smith, R. Lieberman, B. Laughman, J. Moore, W. Brown, J. Haggerty,
971 A. Rockwell, G. Stossmeister, S. Williams, G. Hernandez, D. Murphy, A. Klekociuk,
972 I. Reid, and J. Ma (2016), The deep propagating gravity wave experiment (deepwave):
973 An airborne and ground-based exploration of gravity wave propagation and effects from
974 their sources throughout the lower and middle atmosphere, *Bull. Amer. Meteor. Soc.*,
975 *97*, 425–453, doi:10.1175/BAMS-D-14-00269.1.
976 Fritts, D. C., and M. J. Alexander (2003), Gravity wave dynamics and effects in the
977 middle atmosphere, *Rev. Geophys.*, *41*(1003), doi:10.1029/2001/RG000106.
978 Fritts, D. C., T. S. Lund, K. Wan, and H.-L. Liu (2021), Numerical simulation of mountain
979 waves over the southern andes. part ii: Momentum fluxes and wave-mean-flow interac-

tions, *Journal of the Atmospheric Sciences*, *78*(10), 3069 – 3088, doi:10.1175/JAS-D-20-0207.1.

Gassmann, A. (2019), Analysis of large-scale dynamics and gravity waves under shedding of inactive flow components, *Mon. Wea. Rev.*, *47*, 2861–2876, doi:10.1175/MWR-D-18-0349.1.

Gelaro, R., W. McCarty, M. J. Suárez, R. Todling, A. Molod, L. Takacs, C. A. Randles, A. Darmenov, M. G. Bosilovich, R. Reichle, K. Wargan, L. Coy, R. Cullather, C. Draper, S. Akella, V. Buchard, A. Conaty, A. M. da Silva, W. Gu, G.-K. Kim, R. Koster, R. Lucchesi, D. Merkova, J. E. Nielsen, G. Partyka, S. Pawson, W. Putman, M. Rienecker, S. D. Schubert, M. Sienkiewicz, and B. Zhao (2017), The modern-era retrospective analysis for research and applications, version 2 (merra-2), *Journal of Climate*, *30*(14), 5419 – 5454, doi:10.1175/JCLI-D-16-0758.1.

Gong, J., D. Wu, and S. Eckermann (2012), Gravity wave variances and propagation derived from airs radiances, *Atmos. Chem. Phys.*, *12*, 1701–1720, doi:10.5194/acp-12-1701-2012.

Harvey, V. L., R. B. Pierce, T. Fairlie, and M. H. Hitchman (2002), A climatology of stratospheric polar vortices and anticyclones, *J. Geophys. Res. Atmos.*, *107(D20)*, 4442, doi:10.1029/2001JD001471.

Hauchecorne, A., and M.-L. Chanin (1980), Density and temperature profiles obtained by lidar between 35 and 70 km, *Geophys. Res. Lett.*, *7*(8), 565–568, doi:10.1029/GL007i008p00565.

Heale, C. J., J. B. Snively, A. N. Bhatt, L. Hoffmann, C. C. Stephan, and E. A. Kendall (2019), Multilayer observations and modeling of thunderstorm generated grav-

ity waves over the midwestern united states, *Geoph. Res. Lett.*, *46*, 14,164–14,174, doi: 10.1029/2019GL085934.

Heale, C. J., K. Bossert, S. Vadas, L. Hoffmann, A. Dornbrack, G. Stober, J. B. Snively, and C. Jacobi (2020), Secondary gravity waves generated by breaking mountain waves over europe, *J. Geophys. Res. Atmos.*, *125*, doi:10.1029/2019JD031662.

Hindley, N. P., C. J. Wright, A. M. Gadian, L. Hoffmann, J. K. Hughes, D. R.Jackson, J. C. King, N. J. Mitchell, T. Moffat-Griffin, A. C. Moss, S. B.Vosper, and A. N. Ross (2021), Stratospheric gravity-waves over the mountainous island of South Georgia: testing a high-resolution dynamical model with 3-D satellite observations and radiosondes, *Atmos. Chem. Phys.*, *21*, 7695–7722, doi:10.5194/acp-21-7695-2021.

Hines, C. O. (1960), Internal atmospheric gravity waves at ionospheric heights, *Can. J. Phys.*, *38*, 1441–1481.

Hoffmann, L., X. Xue, and M. J. Alexander (2013), A global view of stratospheric gravity wave hotspots located with Atmospheric Infrared Sounder observations, *J. Geophys. Res. Atmos.*, *118*, 416–434, doi:10.1029/2012JD018658.

Hoffmann, L., A. W. Grimsdell, and M. J. Alexander (2016), Stratospheric gravity waves at southern hemisphere orographic hotspots: 2003-2014 AIRS/Aqua observations, *Atmos. Chem. Phys.*, *16*, 9381–9397, doi:10.5194/acp-16-9381-2016.

Hoffmann, P., and M. Alexander (2009), Retrieval of stratospheric temperatures from atmospheric infrared sounder radiance measurements for gravity wave studies, *J. Geophys. Res.*, *114*, D07,105, doi:10.1029/2008JD011241.

Holt, L. A., M. J. Alexander, and L. C. et al. (2017), An evaluation of gravity waves and gravity wave sources in the southern hemisphere in a 7 km global climate simulation,

Q J R Meteorol Soc., *143(707)*, 2481–2495, doi:10.1002/qj.3101.

Holton, J., and M. Alexander (1999), Gravity waves in the mesosphere generated by tropospheric convection, *Tellus*, *51A-B*, 45–58.

Horinouchi, T., T. Nakamura, and J.-I. Kosaka (2002), Convectively generated mesoscale gravity waves simulated throughout the middle atmosphere, *Geophys. Res. Lett.*, *29(21)*, 2007, doi:10.1029/2002GL016069.

Huang, K. M., A. Z. Liu, S. D. Zhang, F. Yi, C. M. Huang, Y. Gong, Q. Gan, Y. H. Zhang, and R. Wang (2017), Simultaneous upward and downward propagating inertia-gravity waves in the MLT observed at Andes Lidar Observatory, *J. Geophys. Res. Atmos.*, *122*, 2812–2830, doi:10.1002/2016JD026178.

Kaifler, N., B. Kaifler, B. Ehard, S. Gisinger, A. Dörnbrack, M. Rapp, R. Kivi, A. Kozlovsky, M. Lester, and B. Liley (2017), Observational indications of downward-propagating gravity waves in middle atmosphere lidar data, *J. Atmos. Sol. - Terres. Phys.*, *162*, 16–27, doi:10.1016/j.jastp.2017.03.003.

Lane, T. P., M. J. Reeder, and T. L. Clark (2001), Numerical modeling of gravity waves generated by deep tropical convection, *J. Atmos. Sci.*, *58*, 1249–1274.

Lane, T. P., R. D. Sharman, T. L. Clark, and H.-M. Hsu (2003), An investigation of turbulence generation mechanisms above deep convection, *J. Atmos. Sci.*, *60*, 1297–1321, doi:10.1175/1520-0469.

Langenbach, A., G. Baumgarten, J. Fiedler, F.-J. Luebken, C. Savigny, and J. Zalach (2019), Year-round stratospheric aerosol backscatter ratios calculated from lidar measurements above northern norway, *Atmospheric Measurement Techniques*, *12*, 4065–4076, doi:10.5194/amt-12-4065-2019.

1049 Li, J., R. Collins, X. Lu, and B. Williams (2021), Lidar observations of instability and
1050 estimates of vertical eddy diffusivity induced by gravity wave breaking in the arctic
1051 mesosphere, *Journal of Geophysical Research: Atmospheres*, *126*, e2020JD033,450, doi:
1052 10.1029/2020JD033450.

1053 Lindzen, R. S. (1981), Turbulence and stress owing to gravity wave and tidal breakdown,
1054 *J. Geophys. Res.*, *86(C10)*, 9707–9714.

1055 Liu, H.-L., J. M. McInerney, S. Santos, P. H. Lauritzen, M. A. Taylor, and N. M. Pedatella
1056 (2014), Gravity waves simulated by high-resolution Whole Atmosphere Community
1057 Climate Model, *Geophys. Res. Lett.*, *41*, 9106–9112, doi:10.1002/2014GL062468.

1058 Lund, T. S., D. C. Fritts, K. Wan, B. Laughman, and H.-L. Liu (2020), Numerical simula-
1059 tion of mountain waves over the southern andes. part i: Mountain wave and secondary
1060 wave character, evolutions, and breaking, *Journal of the Atmospheric Sciences*, *77*(12),
1061 4337 – 4356, doi:10.1175/JAS-D-19-0356.1.

1062 Luo, Z., and D. C. Fritts (1993), Gravity wave excitation by geostrophic adjustment of
1063 the jet stream, part ii: Three-dimensional forcing, *J. Atmos. Sci.*, *50*, 104–115.

1064 Marks, C. J., and S. D. Eckermann (1995), A three-dimensional nonhydrostatic ray-
1065 tracing model for gravity waves: Formulation and preliminary results for the middle
1066 atmosphere, *J. Atmos. Sci.*, *52*, 1959–1984.

1067 Nicolls, M. J., R. H. Varney, S. L. Vadas, P. A. Stamus, C. J. Heinselman, R. B. Cosgrove,
1068 and M. C. Kelley (2010), Influence of an inertia-gravity wave on mesospheric dynamics:
1069 A case study with the Poker Flat Incoherent Scatter Radar, *J. Geophys. Res.*, *115*,
1070 D00N02, doi:10.1029/2010JD014042.

1071 O'Sullivan, D., and T. J. Dunkerton (1995), Generation of inertia-gravity waves in a
1072 simulated life-cycle of baroclinic instability, *J. Atmos. Sci.*, *52*, 3695–3716.
1073 Pandya, M. J. A., R. E. (1999), Linear stratospheric gravity waves above convective
1074 thermal forcing, *J. Atmos. Sci.*, *56(14)*, 2434–2446.
1075 Piani, C., D. Durran, M. J. Alexander, and J. R. Holton (2000), A numerical study of
1076 three dimensional gravity waves triggered by deep tropical convection, *J. Atmos. Sci.*,
1077 *57*, 3689–3702.
1078 Pitteway, M., and C. Hines (1963), The viscous damping of atmospheric gravity waves,
1079 *Can. J. Phys.*, *41*, 1935–1948.
1080 Plougonven, R., and F. Zhang (2014), Internal gravity waves from atmospheric jets and
1081 fronts, *Rev. Geophys.*, *52*, 33–76, doi:10.1002/2012RG000419.
1082 Plougonven, R., A. Hertzog, and H. Teitelbaum (2008), Observations and simulations of a
1083 large-amplitude mountain wave breaking over the antarctic peninsula, *J. Geophys. Res.*,
1084 *113 (D16113)*, doi:10.1029/2007JD009739.
1085 Sato, K., and M. Yoshiki (2008), Gravity wave generation around the polar vortex in the
1086 stratosphere revealed by 3-hourly radiosonde observations at Syowa Station, *J. Atmos.*
1087 *Sci.*, *65*, 3719–3735, doi:10.1175/2008JAS2539.1.
1088 Sato, K., S. Tanteno, S. Watanabe, and Y. Kawatani (2012), Gravity wave characteristics
1089 in the southern hemisphere revealed by a high-resolution middle-atmosphere general
1090 circulation model, *J. Atmos. Sci.*, *69*, 1378–1396, doi:10.1175/JAS-D-11-0101.1.
1091 Satomura, T., and K. Sato (1999), Secondary generation of gravity waves associated with
1092 the breaking of mountain waves, *J. Atmos. Sci.*, *56*, 3847–3858.

Sawyer, J. S. (1961), Quasi-periodic wind variations with height in the lower stratosphere, *J. Quant. Spectrosc. Ra.*, *87*, 2433, doi:10.1002/qj.49708737104.

Schöch, A., G. Baumgarten, and J. Fiedler (2008), Polar middle atmosphere temperature climatology from rayleigh lidar measurements at alomar (69° n), *Annales Geophysicae*, *26*, doi:10.5194/angeo-26-1681-2008.

Shibuya, R., K. Sato, M. Tsutsumi, T. Sato, Y. Tomikawa, K. Nishimura, and M. Kohma (2017), Quasi-12h inertia-gravity waves in the lower mesosphere observed by the pansy radar at syowa station (39.6e, 69.0s), *Atmos. Chem. Phys.*, *17*, 6455–6476, doi:10.5194/acp-17-6455-2017.

Smith, S., S. Vadas, W. Baggaley, G. Hernandez, and J. Baumgardner (2013), Gravity wave coupling between the mesosphere and thermosphere over new zealand, *J. Geophys. Res.*, *118*, 2694–2707, doi:10.1002/jgra.50263.

Snively, J. B., and V. P. Pasko (2003), Breaking of thunderstorm-generated gravity waves as a source of short-period ducted waves at mesopause altitudes, *Geophys. Res. Lett.*, *30(24)*, 2254, doi:10.1029/2003GL018436.

Song, I.-S., H.-Y. Chun, and P. Lane (2003), Generation mechanisms of convectively forced internal gravity waves and their propagation to the stratosphere, *J. Atmos. Sci.*, *60*, 1960–1980.

Stephan, C., and M. J. Alexander (2015), Realistic simulations of atmospheric gravity waves over the continental u.s. using precipitation radar data, *J. Adv.Model. Earth Syst.*, *7*, 823835, doi:10.1002/2014MS000396.

Strelnikova, I., G. Baumgarten, and F.-J. Lübken (2020), Advanced hodograph-based analysis technique to derive gravity-wave parameters from lidar observations, *Atmos.*

Meas. Tech., *13,*, 479499, doi:10.5194/amt-13-479-2020.

Strelnikova, I., M. Almowafy, G. Baumgarten, K. Baumgarten, M. Gerding, F.-J. Lübken, and M. Ern (2021), Seasonal cycle of gravity wave potential energy densities from lidar and satellite observations at 54n and 69n, *Journal of the Atmospheric Sciences*, *78*, doi:10.1175/JAS-D-20-0247.1.

Taylor, M. J., and M. A. Hapgood (1988), Identification of a thunderstorm as a source of short period gravity waves in the upper atmospheric nightglow emissions, *Planet. Space Sci.*, *36*, 975.

Vadas, S. L. (2007), Horizontal and vertical propagation and dissipation of gravity waves in the thermosphere from lower atmospheric and thermospheric sources, *J. Geophys. Res.*, *112*, doi:10.1029/2006JA011845.

Vadas, S. L. (2013), Compressible *f*-plane solutions to body forces, heatings, and coolings, and application to the primary and secondary gravity waves generated by a deep convective plume, *J. Geophys. Res.: Space Physics*, *118*, 2377–2397, doi:10.1002/jgra.50163.

Vadas, S. L., and E. Becker (2018), Numerical modeling of the excitation, propagation, and dissipation of primary and secondary gravity waves during wintertime at McMurdo Station in the Antarctic, *J. Geophys. Res. Atmos.*, *123*, 9326–9369, doi:10.1029/2017JD027974.

Vadas, S. L., and E. Becker (2019), Numerical modeling of the generation of tertiary gravity waves in the mesosphere and thermosphere during strong mountain wave events over the Southern Andes, *J. Geophys. Res. Space Phys.*, *124*, 7687–7718, doi:10.1029/2019JA026694.

Vadas, S. L., and G. Crowley (2010), Sources of the traveling ionospheric disturbances observed by the ionospheric TIDDBIT sounder near Wallops Island on October 30, 2007, *J. Geophys. Res. Space Physics*, *115*, A07324, doi:10.1029/2009JA015053.

Vadas, S. L., and G. Crowley (2017), Neutral wind and density perturbations in the thermosphere created by gravity waves observed by the TIDDBIT sounder, *J. Geophys. Res. Space Physics*, *122*, 6652–6678, doi:10.1002/2016JA023828.

Vadas, S. L., and D. C. Fritts (2001), Gravity wave radiation and mean responses to local body forces in the atmosphere, *J. Atmos. Sci.*, *58*, 2249–2279.

Vadas, S. L., and D. C. Fritts (2005), Thermospheric responses to gravity waves: Influences of increasing viscosity and thermal diffusivity, *J. Geophys. Res.*, *110*, D15103, doi: 10.1029/2004JD005574.

Vadas, S. L., and H.-L. Liu (2009), Generation of large-scale gravity waves and neutral winds in the thermosphere from the dissipation of convectively generated gravity waves, *J. Geophys. Res.*, *114*, A10310, doi:10.1029/2009JA014108.

Vadas, S. L., and H.-L. Liu (2013), Numerical modeling of the large-scale neutral and plasma responses to the body forces created by the dissipation of gravity waves from 6 h of deep convection in Brazil, *J. Geophys. Res.*, *118*, 2593–2617, doi:10.1002/jgra.50249.

Vadas, S. L., and M. J. Nicolls (2012), The phases and amplitudes of gravity waves propagating and dissipating in the thermosphere: Theory, *J. Geophys. Res*, *117*(A05322), doi:10.1029/2011JA017426.

Vadas, S. L., D. C. Fritts, and M. J. Alexander (2003), Mechanisms for the generation of secondary waves in wave breaking regions, *J. Atmos. Sci.*, *60*, 194–214, doi: 10.1029/2004JD005574.

1161 Vadas, S. L., M. J. Taylor, P.-D. Pautet, P. A. Stamus, D. C. Fritts, H.-L. Liu, F. T. S.
1162 Sabbas, V. T. Rampinelli, P. Batista, and H. Takahashi (2009a), Convection: the likely
1163 source of medium-scale gravity waves observed in the OH airglow layer near Basilia,
1164 Brazil, during the spreadfex campaign, *Ann. Geophys.*, *27*, 231–259.

1165 Vadas, S. L., J. Yue, C.-Y. She, P. Stamus, and A. Liu (2009b), A model study of the
1166 effects of winds on concentric rings of gravity waves from a convective plume near Fort
1167 Collins on 11 May 2004, *J. Geophys. Res.*, *114*, D06,103, doi:10.1029/2008JD010753.

1168 Vadas, S. L., J. Zhao, X. Chu, and E. Becker (2018), The excitation of secondary gravity
1169 waves from local body forces: Theory and observation, *J. Geophys. Res. Atmos.*, *123*,
1170 9296–9325, doi:10.1029/2017JD027970.

1171 von Zahn, U., G. Cossart, J. Fiedler, K. Fricke, G. Nelke, G. Baumgarten, D. Rees,
1172 A. Hauchecorne, and K. Adolfsen (2000), The ALOMAR Rayleigh/Mie/Raman li-
1173 dar: Objectives, configuration, and performance, *Annales Geophysicae*, *18*, doi:
1174 10.1007/s00585-000-0815-2.

1175 Walterscheid, R., L. Gelinas, C. Mechoso, and G. Schubert (2016), Spectral distri-
1176 bution of gravity wave momentum fluxes over the antarctic peninsula from con-
1177 cordiasi superpressure balloon data, *J. Geophys. Res. Atmos.*, *121*, 7509–7527, doi:
1178 10.1002/2015JD024253.

1179 Walterscheid, R. L., G. Schubert, and D. G. Brinkman (2001), Small-scale gravity waves
1180 in the upper mesosphere and lower thermosphere generated by deep tropical convection,
1181 *J. Geophys. Res.*, *106*, 31,825–31,832.

1182 Wang, L., and M. A. Geller (2003), Morphology of gravity-wave energy as observed from
1183 4 years (19982001) of high vertical resolution u.s. radiosonde data, *J. Geophys. Res.-*

Atmos., *108*, 4489, doi:10.1029/2002JD002786.

Watanabe, S., K. Sato, and M. Takahashi (2006), A general circulation model study of the orographic gravity waves over Antarctica excited by katabatic winds, *J. Geophys. Res.*, *111*(D18104), doi:10.1029/2005JD006851.

Watanabe, S., Y. Kawatani, Y. Tomikawa, K. Miyazaki, M. Takahashi, and K. Sato (2008), General aspects of a T213L256 middle atmosphere general circulation model, *J. Geophys. Res.*, *113*, doi:10.1029/2008JD010026.

Yoshiki, M., and K. Sato (2000), A statistical study of gravity waves in the polar regions based on operational radiosonde data, *J. Geophys. Res.*, *105*, 17,995–18,011.

Yoshiki, M., N. Kizu, and K. Sato (2004), Energy enhancements of gravity waves in the antarctic lower stratosphere associated with variations in the polar vortex and tropospheric disturbances, *J. Geophys. Res.*, *109*, D23,104, doi:10.1029/2004JD004870.

Yue, J., S. L. Vadas, C.-Y. She, T. Nakamura, S. C. Reising, H.-L. Liu, P. Stamus, D. A. Krueger, W. Lyons, , and T. Li (2009), Concentric gravity waves in the mesosphere generated by deep convective plumes in the lower atmosphere near Fort Collins, *J. Geophys. Res.*, *114*, D06104, doi:10.1029/2008JD011244.

Zhang, F., S. Wang, and R. Plougonven (2004), Uncertainties in using the hodograph method to retrieve gravity wave characteristics from individual soundings, *Geophys. Res. Lett.*, *31*, L11,110, doi:10.1029/2004GL019841.

Zhao, J., X. Chu, C. Chen, X. Lu, W. Fong, Z. Yu, R. M. Jones, B. R. Roberts, and A. Dörnbrack (2017), Lidar observations of stratospheric gravity waves from 2011 to 2015 at McMurdo (77.84°S, 166.69°E), Antarctica: 1. Vertical wavelengths, periods, and frequency and vertical wavenumber spectra, *J. Geophys. Res. Atmos.*, *122*, doi:

10.1002/2016JD026368.

Zülicke, C., and D. H. W. Peters (2006), Simulation of inertia-gravity waves in a poleward breaking rossby wave, *J. Atmos. Sci.*, *63*, 3253–3276, doi:10.1175/JAS3805.1.

Zülicke, C., and D. H. W. Peters (2008), Parameterization of strong stratospheric inertia gravity waves forced by poleward breaking rossby waves, *Mon. Wea. Rev.*, *136*, 98–119, doi:10.1175/2007MWR2060.1.

Table 1. Alternative Method: Intrinsic Parameters of Secondary GWs over ALOMAR

	PSD of T'		Parameters using GW Dispersion and Polarization Relations				
Event	$\lvert\lambda_z\rvert$ (km)	$\lvert\tau_r\rvert$ (h)	λ_H (km)	τ_{Ir} (h)	c_H (m/s)	c_{IH} (m/s)	ψ(deg)
# 1	15.3 ± 4.7	6.7 ± 1.7	477.2 ± 279.5	2.8 ± 0.9	20.0 ± 9.5	48.2 ± 9.4	134.7 ± 8.1
# 2	12.3 ± 3.5	8.3 ± 2.0	1471.5 ± 227.7	7.6 ± 0.6	57.9 ± 16.6	52.1 ± 10.3	90.9 ± 7.9

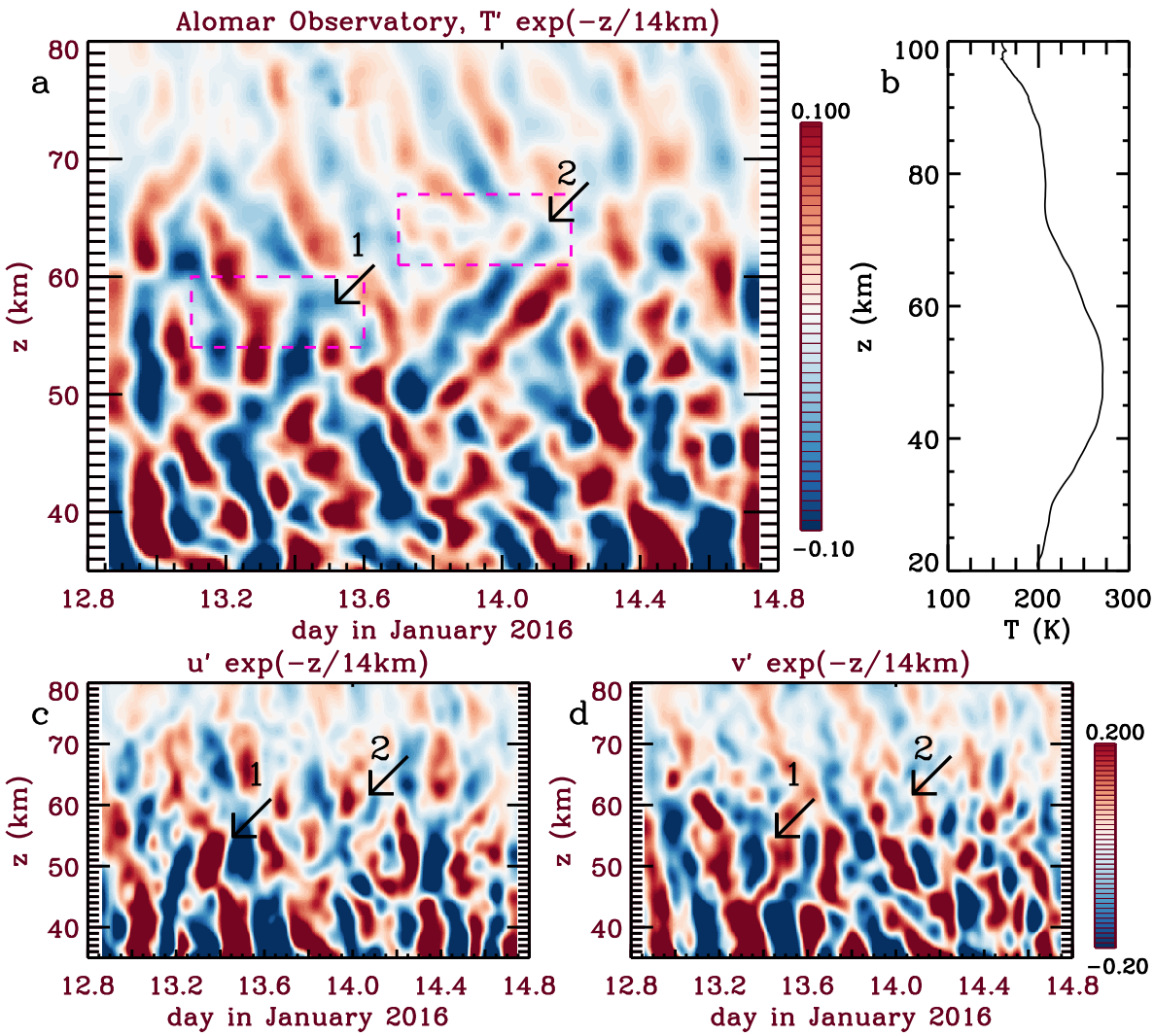

Figure 1. Lidar observations at the ALOMAR on 12-14 January 2016. (a) Scaled temperature perturbations, $T' \exp(-z/14\text{km})$ (colors, in K). The pink dash rectangles show the altitude ranges where the downward GWs are generated during events #1 and #2 (see text). (b) Background temperature, $\overline{T}$ (in K). (c) Scaled zonal wind perturbations, $u' \exp(-z/14\text{km})$ (colors, in m/s). (d) Scaled meridional wind perturbations, $v' \exp(-z/14\text{km})$ (colors, in m/s). The perturbations are filtered to retain GWs with $1 < \tau_r < 11$ h and $|\lambda_z| \geq 1$ km. The black arrows point at z_{knee} for events #1 and #2. The colors are oversaturated to better see the GWs at $45 < z < 80$ km.

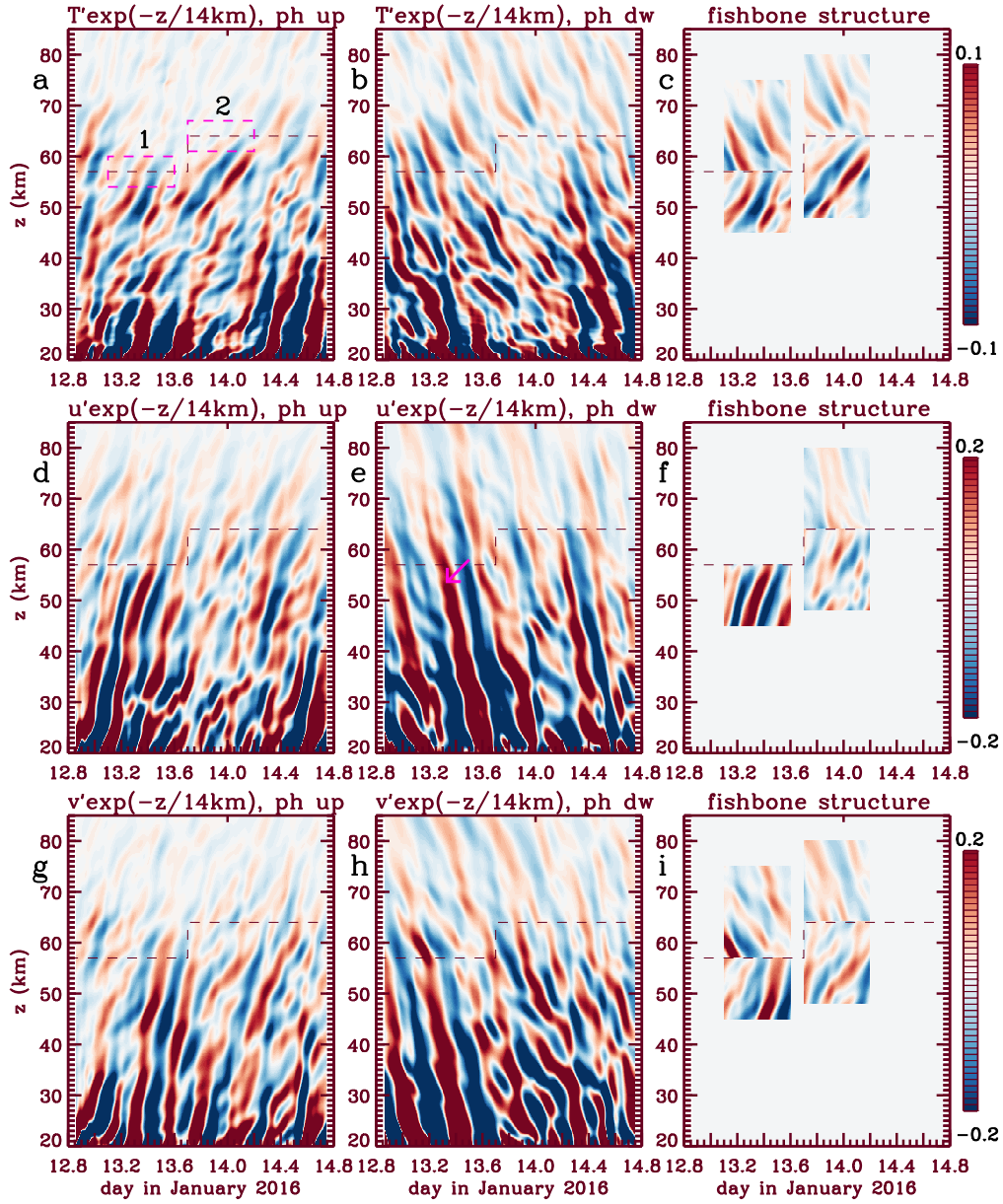

Figure 2. Lidar observations at ALOMAR on 12-14 January. (a) $T'\exp(-z/14\text{km})$ (colors, in K) for GWs with upgoing phases in time. The pink dash rectangles are the same as in Fig. 1a. (b) Same as (a) for GWs with downgoing phases in time. (c) Same as (a-b) but for GWs having upgoing (downgoing) phases below (above) z_{knee} during the time and altitude boundaries for each event (see text). The dashed lines show $z_{\text{knee}} = 57$ km before 13.7 January and $z_{\text{knee}} = 64$ km after 13.7 January. Rows 2-3: Same as the first row but for $u'\exp(-z/14\text{km})$ and $v'\exp(-z/14\text{km})$, respectively (in m/s). The colors are oversaturated to better see the GWs at $45 < z < 80$ km.

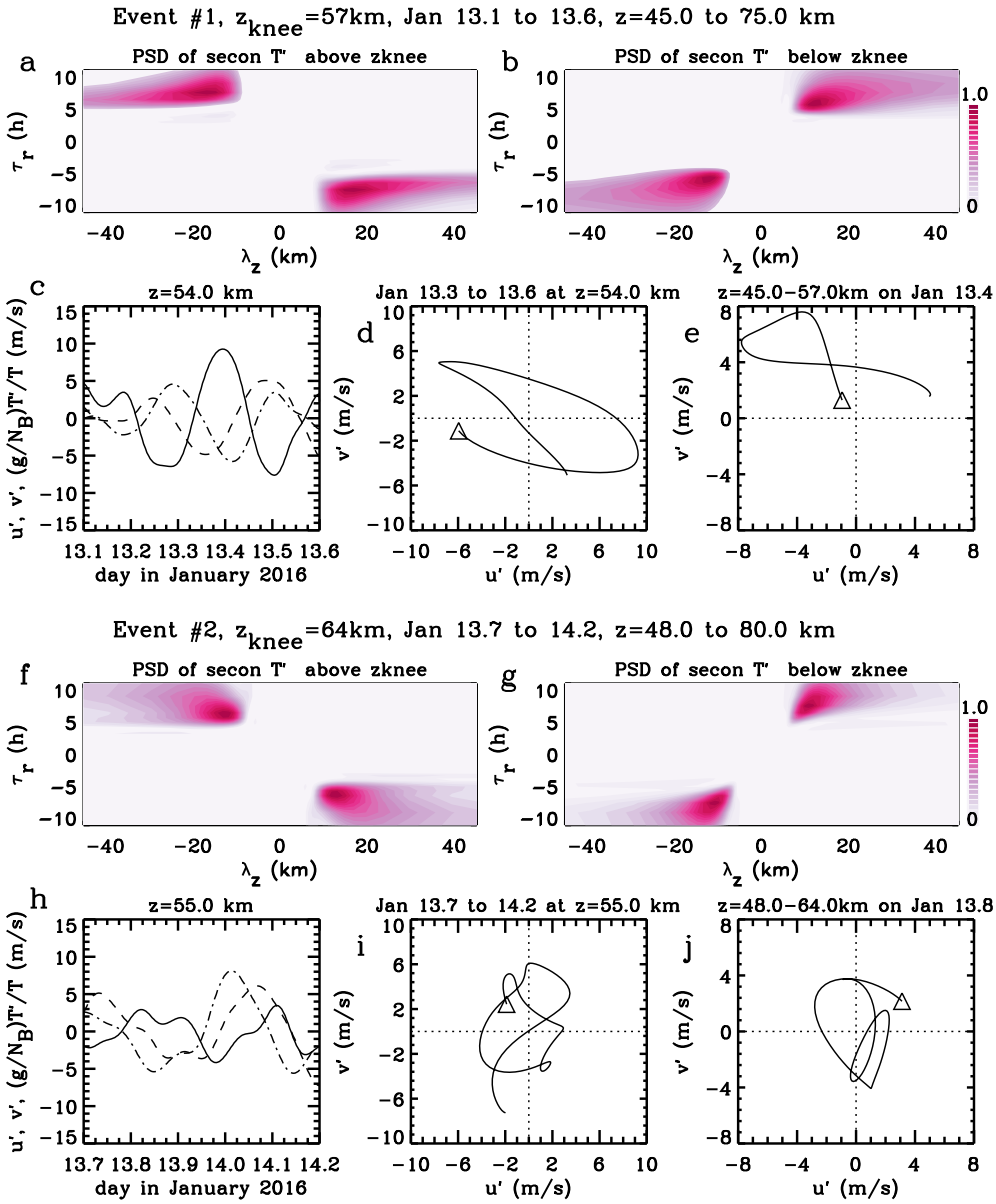

Figure 3. Lidar observations at ALOMAR on 13-14 January. (a)-(e): Event # 1. (a),(b) PSD of T' from Fig. 2c, $|T'|^2$, above and below $z_{\rm knee} = 57$ km, respectively, within the event boundaries (colors). (c) u' (solid), v' (dashed), and $(g/N_B)T'/\overline{T}$ (dashed-dotted) (in m/s) at $z = 54$ km. (d) u' versus v' for 13.3-13.6 January (triangle at 13.3 Jan) at $z = 54$ km. (e) u' versus v' for $z = 45 - 57$ km on Jan 13.4 (triangle at $z = 45$ km). (f)-(j): Same as (a)-(e) but for event # 2 with $z_{\rm knee} = 64$ km with the following changes: (h): $z = 55$ km. (i): u' versus v' for 13.7-14.2 January (triangle at 13.7 Jan) at $z = 55$ km. (j): u' versus v' for $z = 48 - 64$ km on Jan 13.8 (triangle at $z = 48$ km).

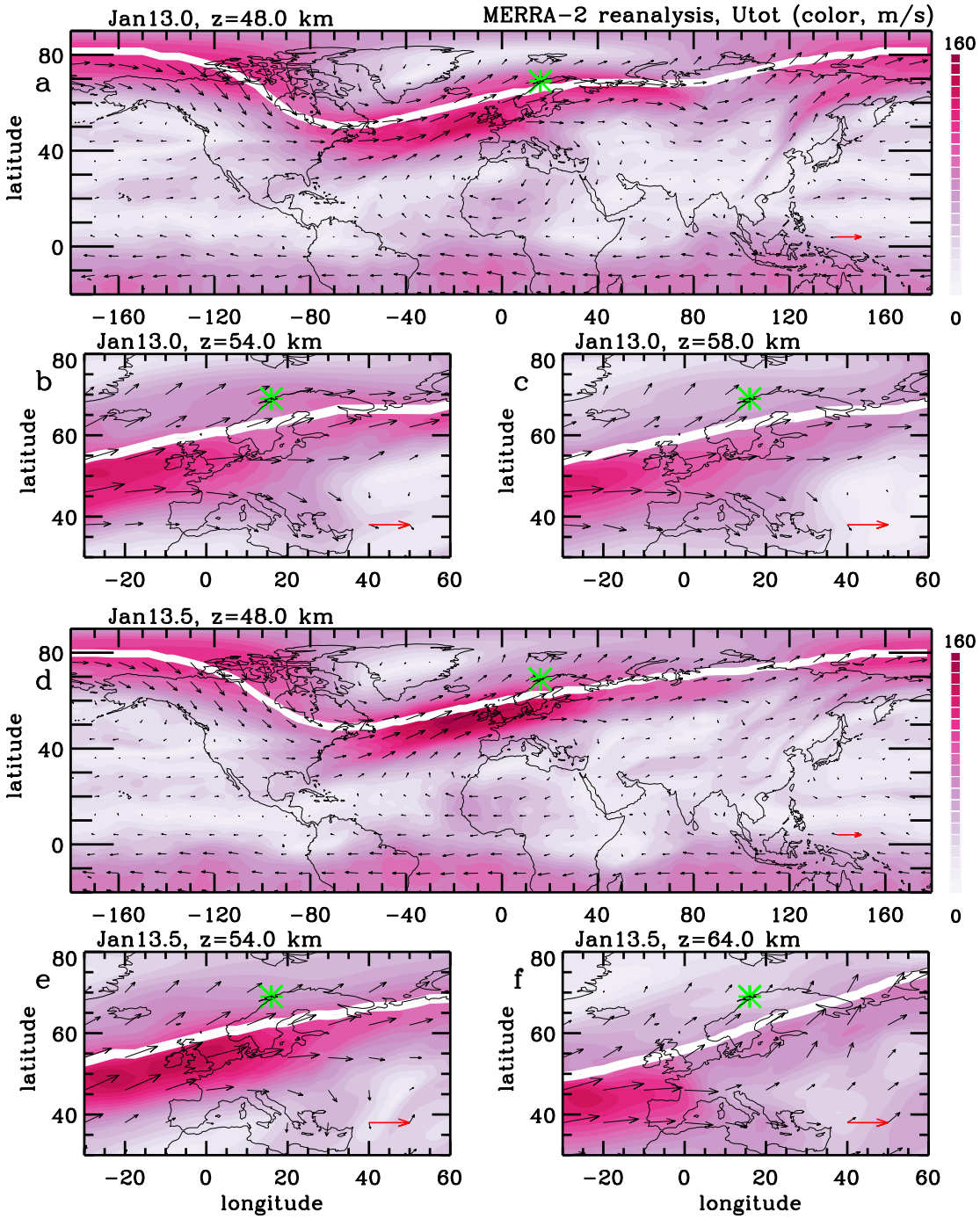

Figure 4. Horizontal wind from MERRA-2 reanalysis (vectors, in m/s). The colors show the magnitude of the horizontal wind, U_{tot} (in m/s). (a-c): January 13.0. a) $z = 48$ km. b) $z = 54$ km. c) $z = 58$ km. (d-f): January 13.5. d) $z = 48$ km. e) $z = 54$ km. f) $z = 64$ km. The red arrows show an eastward wind vector with $U_{tot} = 100$ m/s. The green asterisks show ALOMAR. The white lines show the vortex edge.

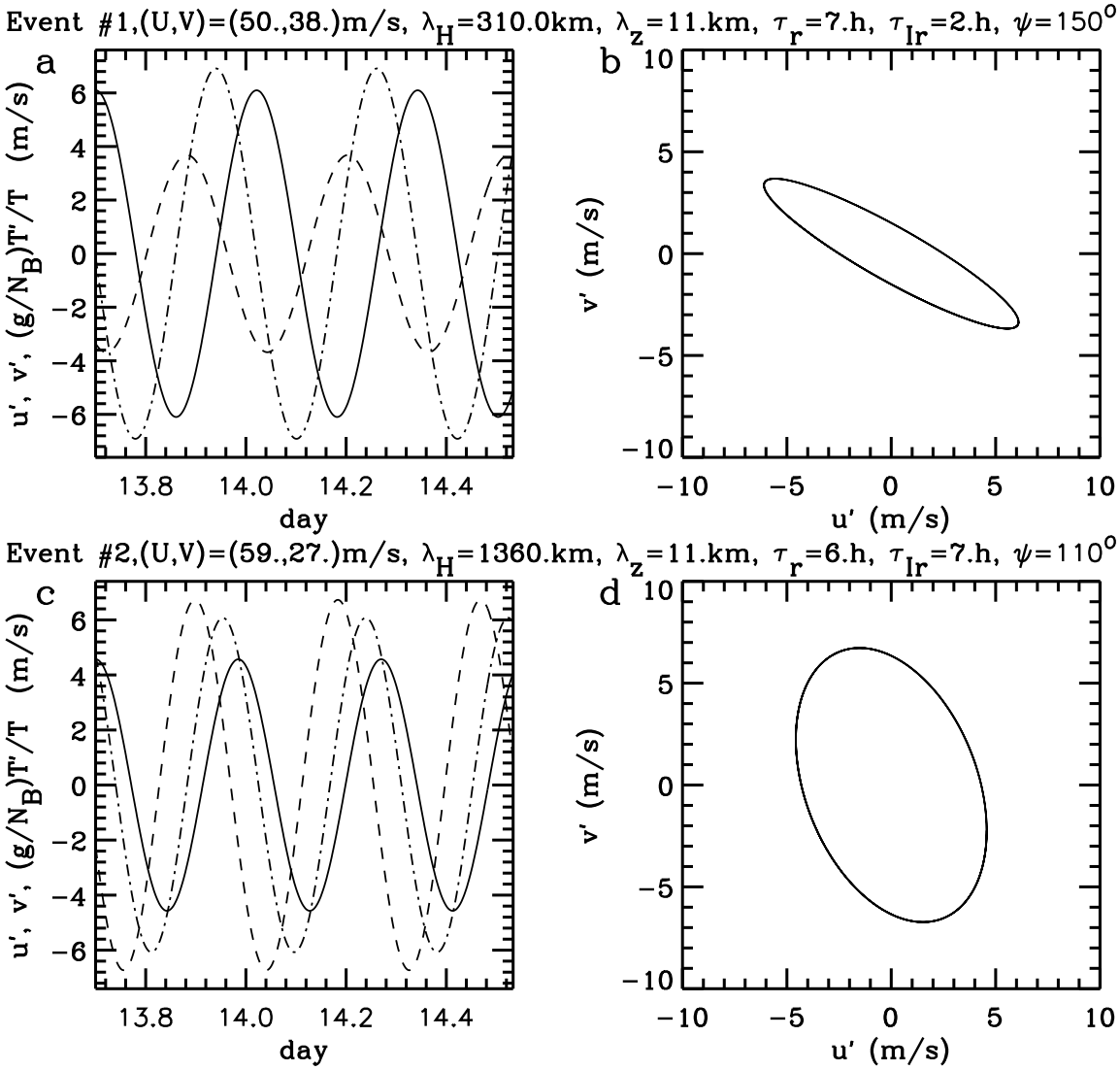

Figure 5. Theoretical solutions to the GW polarization and dispersion relations for monochromatic GWs. (a) u' (solid line), v' (dashed line), and $(g/N_B)T'/\overline{T}$ (dashed-dotted line) (in m/s) for a possible event #1 GW with $\lambda_H = 310$ km, $\lambda_z = 11$ km, $\tau_r = 7$ h, $\tau_{Ir} = 2$ h and $\psi = 150°$. (b) Hodograph of u' versus v' in time. (c-d): Same as (a-b), but for a possible event #2 GW with $\lambda_H = 1360$ km, $\lambda_z = 11$ km, $\tau_r = 6$ h, $\tau_{Ir} = 7$ h and $\psi = 110°$. The background wind is obtained from MERRA-2 reanalysis at the location of ALOMAR. Row 1: $(U, V) = (50, 38)$ m/s at $z = 54$ km at 6 UT on 13 January. Row 2: $(U, V) = (59, 27)$ m/s at $z = 55$ km at 0 UT on 14 January.

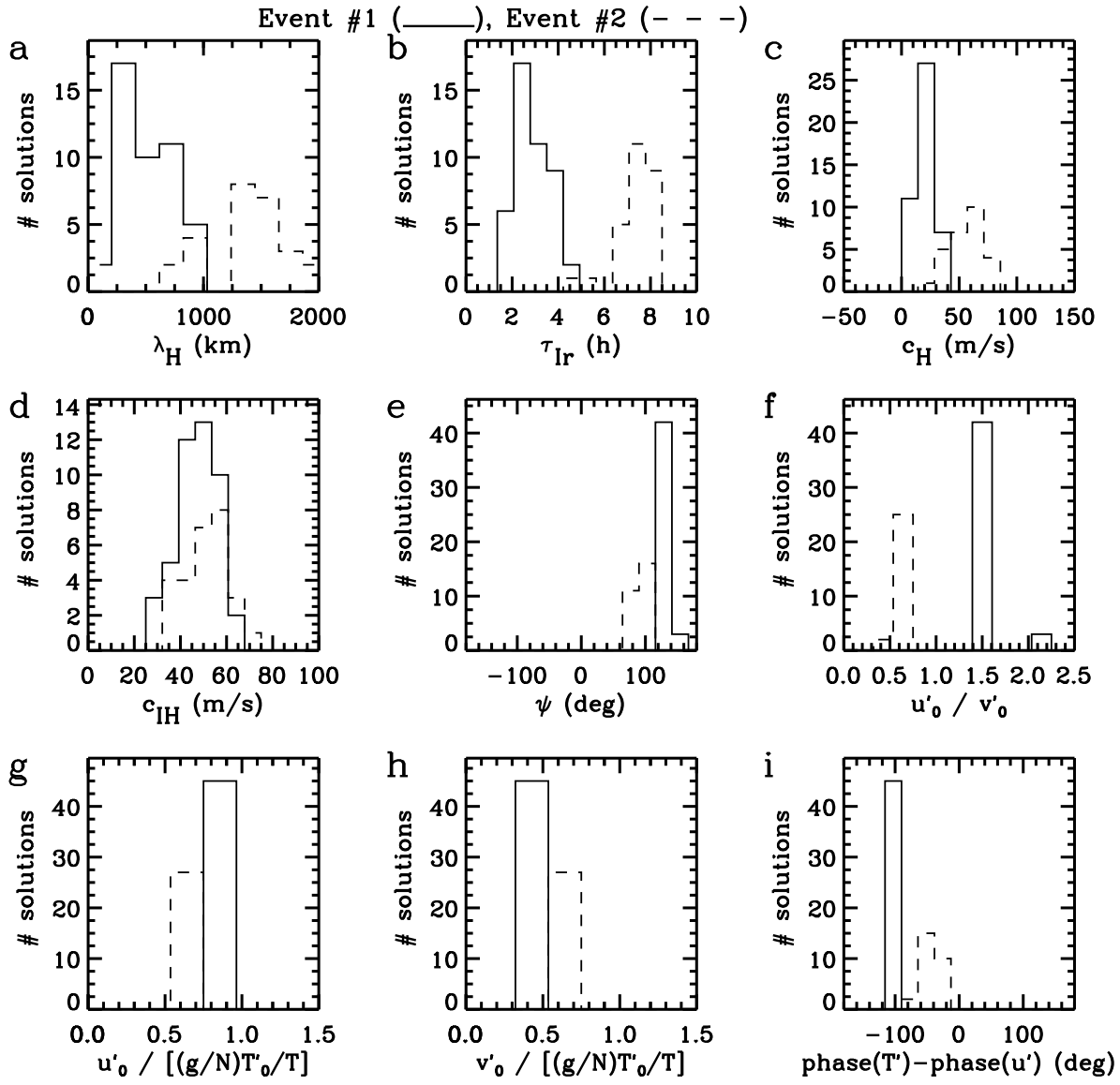

Figure 6. Number of viable GW solutions to the f-plane compressible polarization and dispersion relations for ALOMAR lidar events #1 (solid line) and #2 (dashed line) as functions of a) λ_H, b) τ_{Ir}, c) c_H, d) c_{IH}, e) ψ, f) u_0'/v_0', g) $u_0'/[(g/N_B)T_0'/\overline{T}]$, h) $v_0'/[(g/N_B)T_0'/\overline{T}]$, i) phase $(T')-$phase (u').

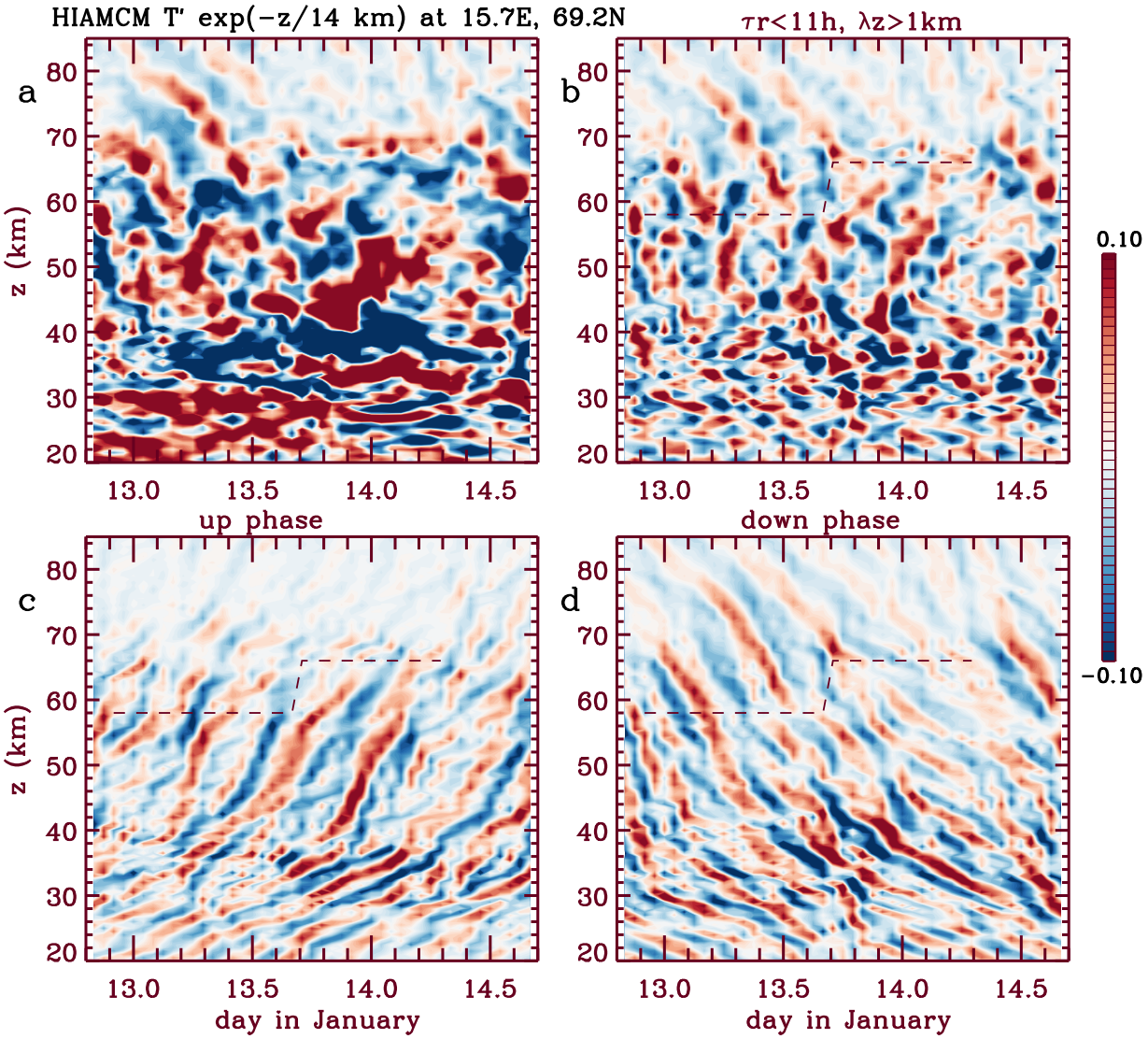

Figure 7. a) Scaled temperature perturbations, $T' \exp(-z/14\,\mathrm{km})$ (colors, in K), from the nudged HIAMCM on 12-14 January over ALOMAR. b) Same as a) but filtered to retain GWs with $\tau_r \leq 11$ hr and $|\lambda_z| \geq 1$ km. c) GWs from (b) with upgoing phases in time. d) GWs from (b) with downgoing phases in time. The dashed lines show z_{knee} during the time and altitude boundaries for events #1 and #2 (see text). The colors are oversaturated in a) to better see the GWs at $45 < z < 80$ km.

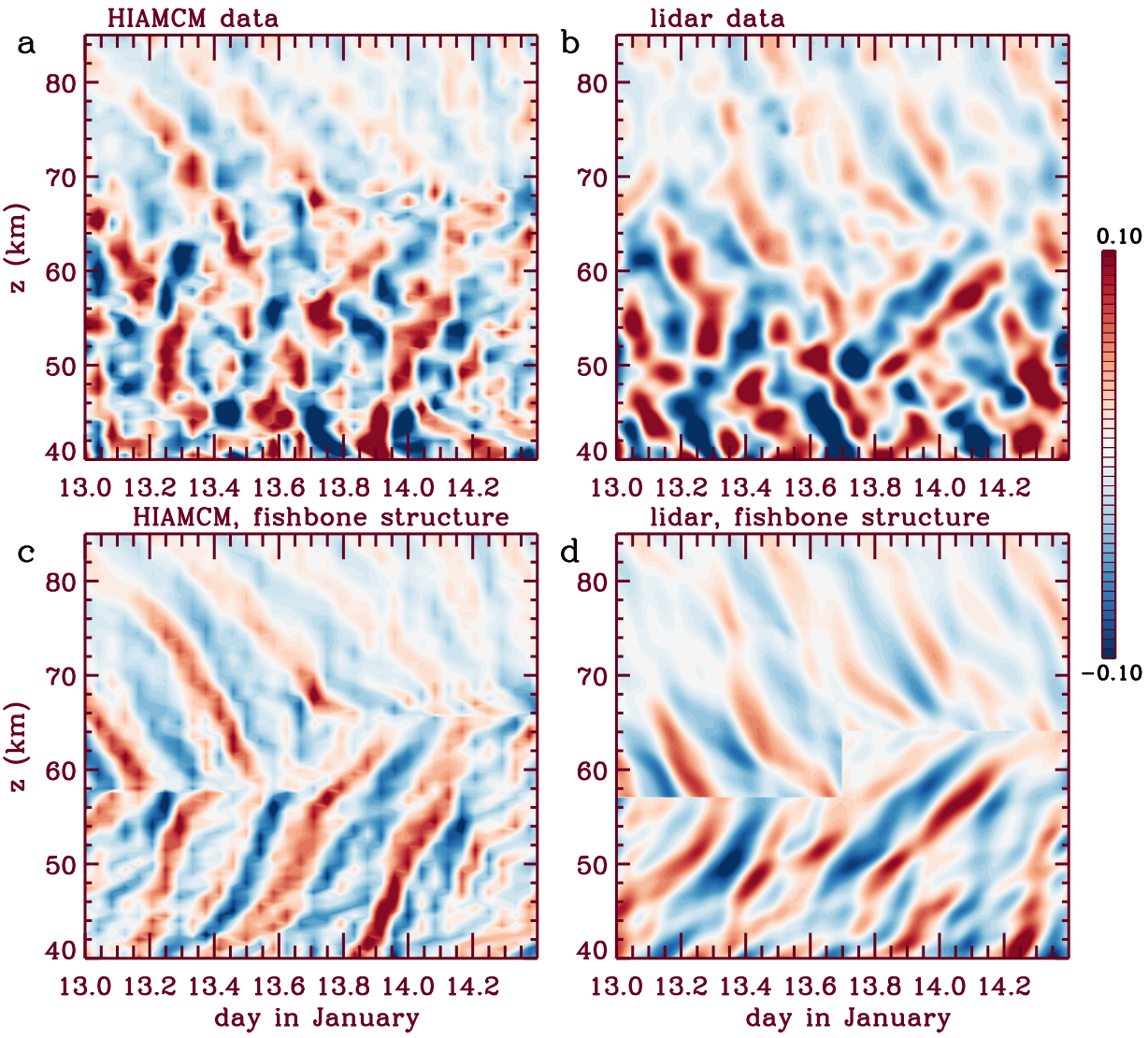

Figure 8. Scaled temperature perturbations, $T' \exp(-z/14\text{km})$ (colors, in K) on 12-14 January 2016. The left column shows the HIAMCM data, while the right column shows the ALOMAR lidar data. Row 1: All GWs. Row 2: GWs with downgoing (upgoing) phases in time above (below) z_{knee} during events #1 and #2.

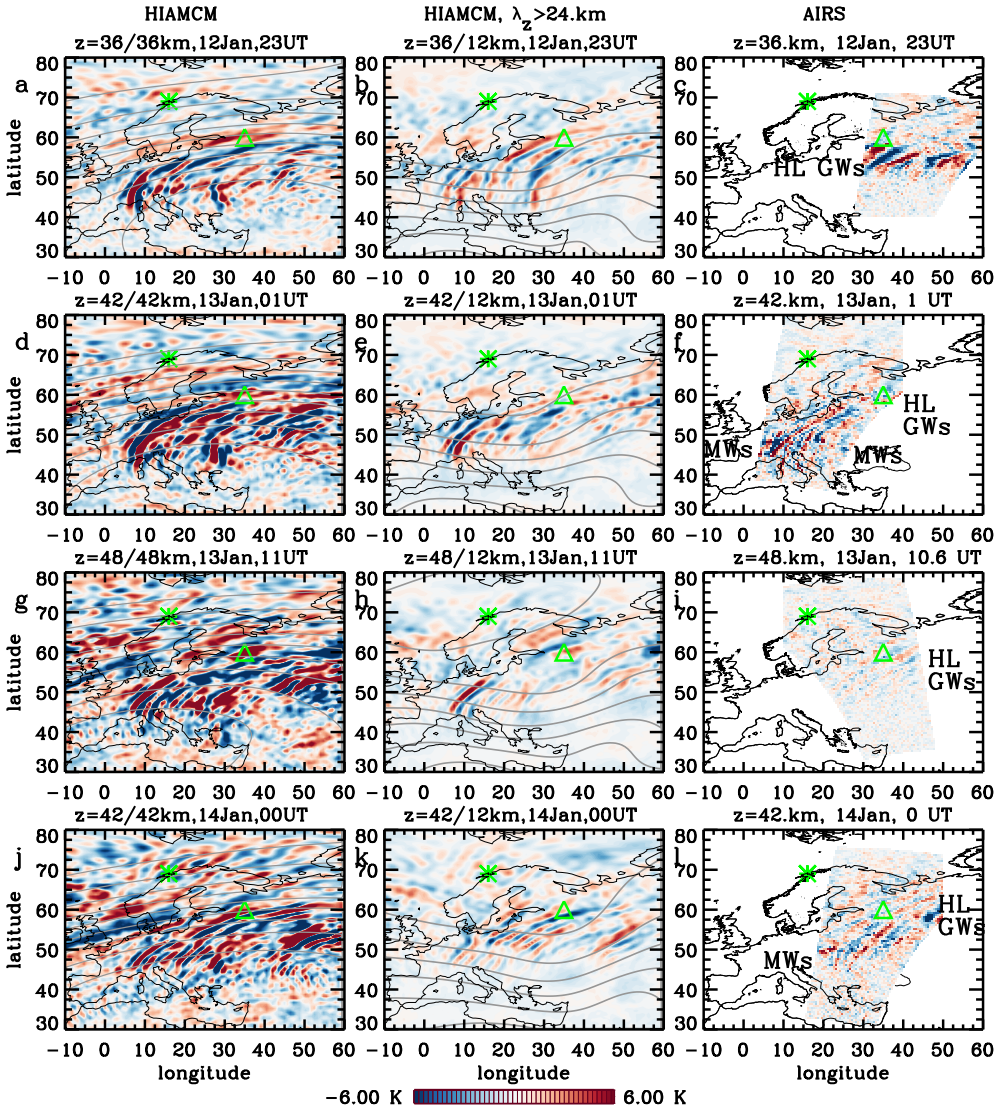

Figure 9. T' (colors, in K). Row 1: 23 UT on Jan 12 at $z = 36$ km. Row 2: 1 UT on Jan 13 at $z = 42$ km. Row 3: 11 UT on Jan 13 at $z = 48$ km. Row 4: 0 UT on Jan 14 at $z = 42$ km. The left column shows the HIAMCM GWs and large-scale horizontal streamfunction (grey lines) at the same times and altitudes. The middle column is the same as the left column except 1) filtered to remove GWs with $|\lambda_z| < 24$ km, and 2) the stream function is shown at $z = 12$ km. The right column shows the AIRS GWs. Labels show the MWs and high-latitude ("HL") GWs. The green asterisks and triangles show ALOMAR and the event #1 LBF. The colors are oversaturated in column 1 to better see the GWs in column 2.

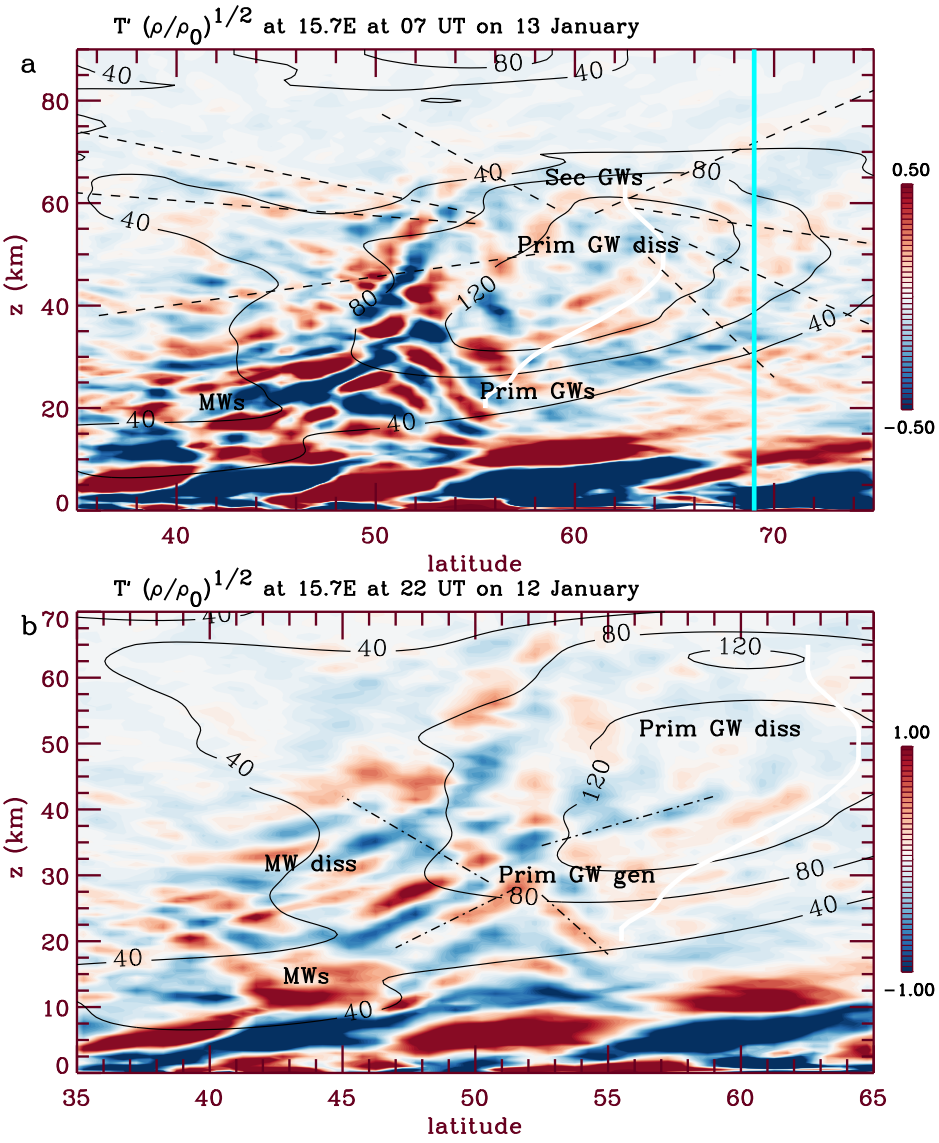

Figure 10. a) $T'\sqrt{\overline{\rho}/\rho_0}$ (colors, in K) as a function of latitude at 15.7° E at 07 UT on 13 January 2016 from the HIAMCM during event #1, where $\rho_0 = 1241\,\mathrm{g/m^3}$. The dash lines highlight secondary GW phase lines. The solid black lines show U_{tot} (in m/s). b) Same as in a) but at 22 UT on 12 January with a larger color scale and for different latitude and altitude ranges to better see the primary GWs. The dash-dot lines highlight primary GW phase lines. Labels show MWs, primary and secondary GWs, as well as generation ("gen") and dissipation ("diss") regions. The turquoise line shows ALOMAR, and the white lines show the edge of the polar vortex. The colors are oversaturated to better see the GWs.

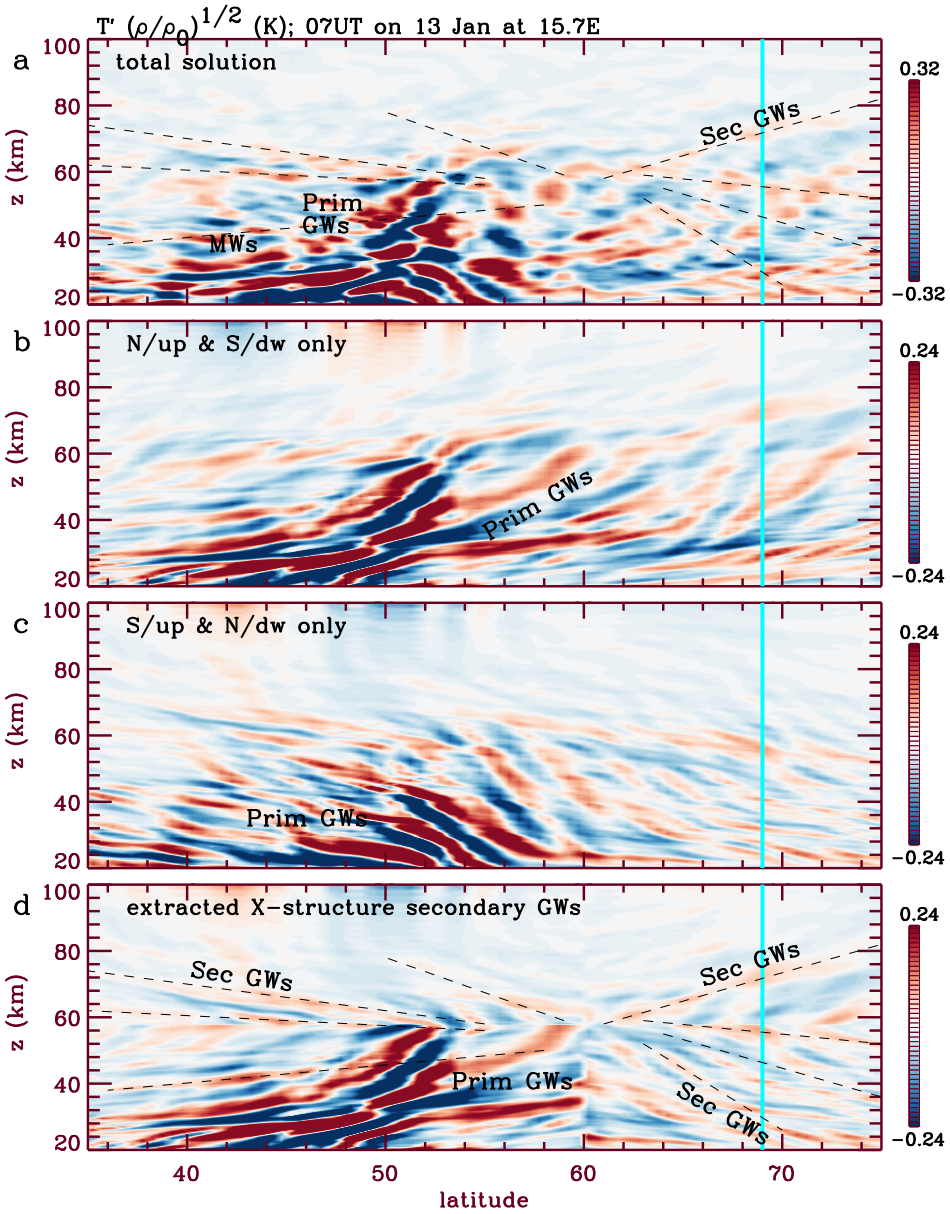

Figure 11. $T'\sqrt{\overline{\rho}/\rho_0}$ from the HIAMCM (colors, in K) as a function of latitude at 07 UT on 13 January at 15.7° E during event #1, where $\rho_0 = 1241\,\mathrm{g/m^3}$. a) Total solution. b) Northward/upward and southward/downward GWs. c) Southward/upward and northward/downward GWs. d) Extracted X-structure of the secondary GWs in event #1. The center of the structure is at $z_{\mathrm{knee}} = 58$ km and $\theta_{\mathrm{cen}} = 60°$ N. Upward/northward primary GWs contaminate the structure at $40 - 60°$ N and $z = 20 - 60$ km in d). Dash lines show the secondary GW phase lines, and are the same as in Fig. 10a. The turquoise lines show ALOMAR. The colors are oversaturated to better see the secondary GWs.

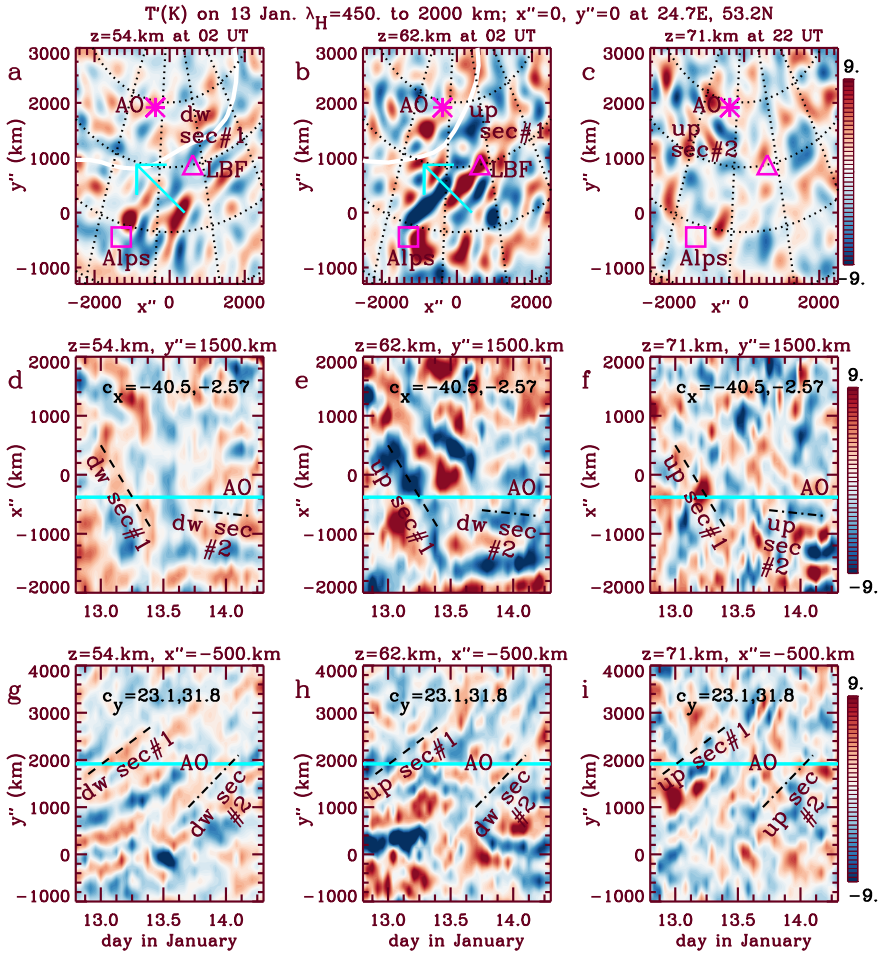

Figure 12. T' (colors, in K) from the HIAMCM for $450 < \lambda_H < 2000$ km on a 2D Cartesian grid with coordinates (x'', y'') parallel to the Earth's surface at 24.7° E and 53.2° N ($x'' = y'' = 0$). Left to right columns show $z = 54$, 62 and 71 km, respectively. a-c) Horizontal slices at 2, 2 and 22 UT on 13 January, respectively. ALOMAR ("AO", asterisks), the northern edge of the Alps at 8° E, 48° N (squares), and the event #1 LBF at 35° E, 60° N ("LBF", triangles) are shown. Turquoise arrows show the approximate propagation direction of the downward ("dw") and upward ("up") event #1 GWs and and white lines show the vortex edge in a-b). Dotted lines show 0 to 60° E in 20° increments and $50 - 70$° N in 10° increments. d-f) Keograms of x'' versus time at $y'' = 1500$ km. g-i): Keograms of y'' versus time at $x'' = -500$ km. Dash (dash-dot) lines indicate event #1 (#2) GWs. ALOMAR is shown by the turquoise lines. c_x and c_y are listed (in m/s). The colors are over-saturated to see the secondary GWs.

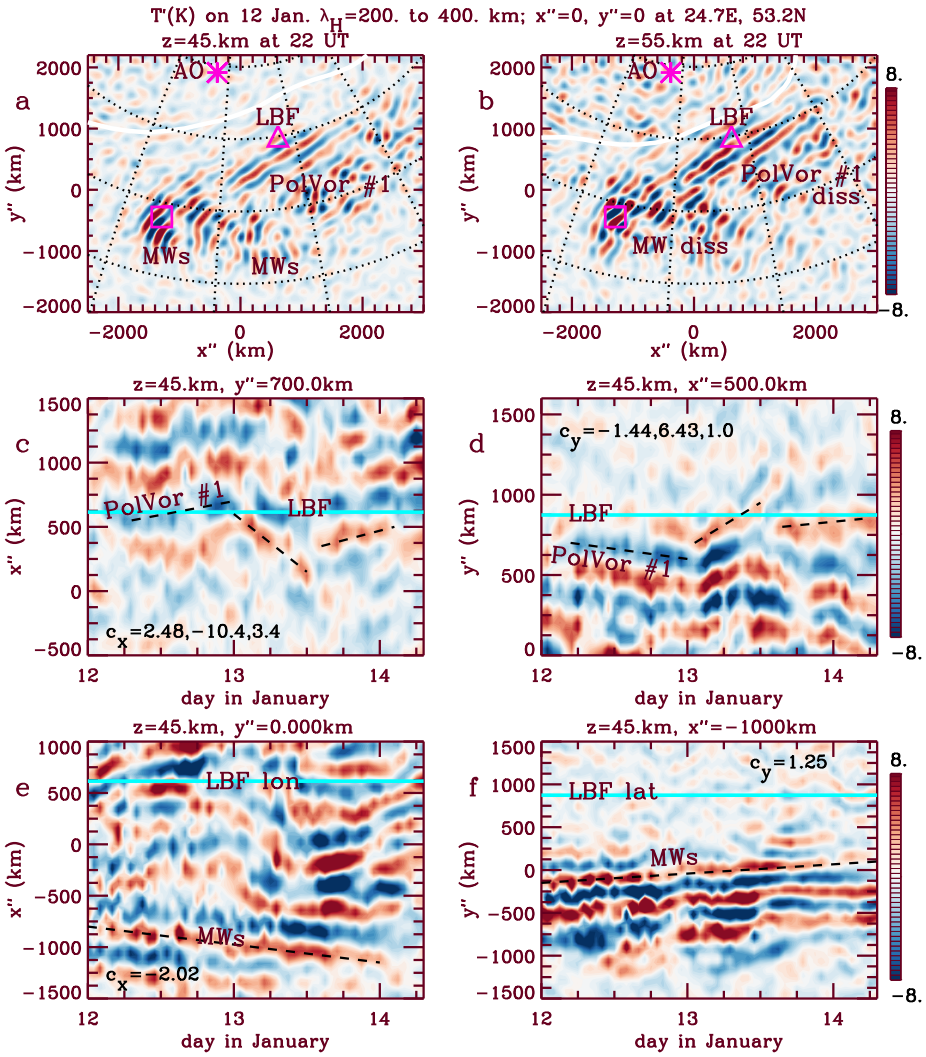

Figure 13. T' (colors, in K) from the HIAMCM for $200 < \lambda_H < 400$ km on a 2D Cartesian grid (with coordinates (x'', y'') parallel to Earth's surface at 24.7° E and 53.2° N ($x'' = y'' = 0$). Horizontal slices at (a) $z = 45$ km and (b) $z = 55$ km at 22 UT on 12 January. The asterisks, squares, triangles, dotted lines, and white lines are the same as in Fig. 12a-b. The propagating and dissipating ("diss") MWs and GWs from the polar vortex ("PolVor") are labeled. c) x'' versus time at $y'' = 700$ km. d): y'' versus time at $x'' = 500$ km. e) x'' versus time at $y'' = 0$ km. f): y'' versus time at $x'' = -1000$ km. Dashed lines indicate the phase lines of the GWs of interest. c_x and c_y are listed (in m/s). The LBF is shown in (c-d) (turquoise lines). The longitude and latitude of the LBF are shown in e)-f), respectively (turquoise lines).

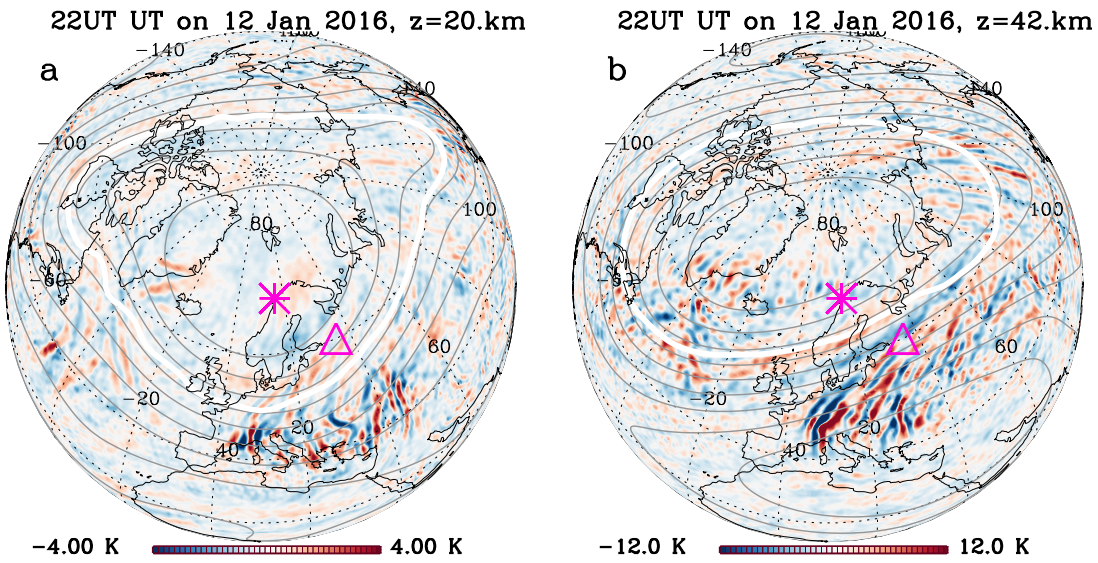

Figure 14. Global view of T' (colors, in K) and the large-scale horizontal streamfunction (grey lines) from the HIAMCM at 22 UT on 12 January. (a) $z = 20$ km. (b) $z = 42$ km. The purple asterisks and triangles show ALOMAR and the event #1 LBF at 35° E and 60° N, respectively. The white lines show the vortex edge.

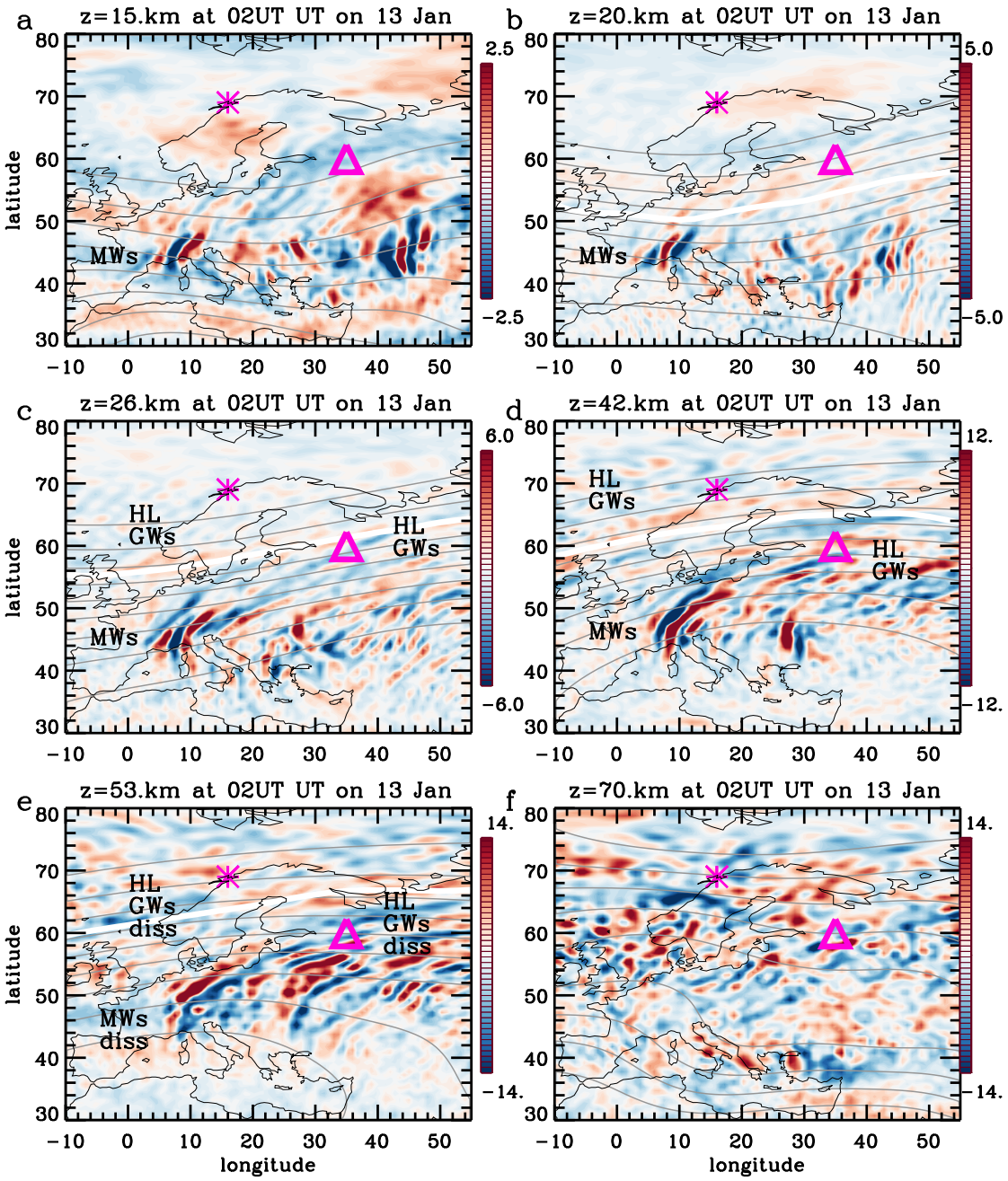

Figure 15. T' (colors, in K) and the large-scale horizontal streamfunction (grey lines) from the HIAMCM at 2 UT on 13 January. (a) $z = 15$ km. (b) $z = 20$ km. (c) $z = 26$ km. (d) $z = 42$ km. (e) $z = 53$ km. (f) $z = 70$ km. The asterisks show ALOMAR and the triangles show the event #1 LBF at 35° E and 60° N. Labels show propagating and dissipating ("diss") MWs and high-latitude ("HL") GWs. The vortex edge is shown as white lines in a)-e).

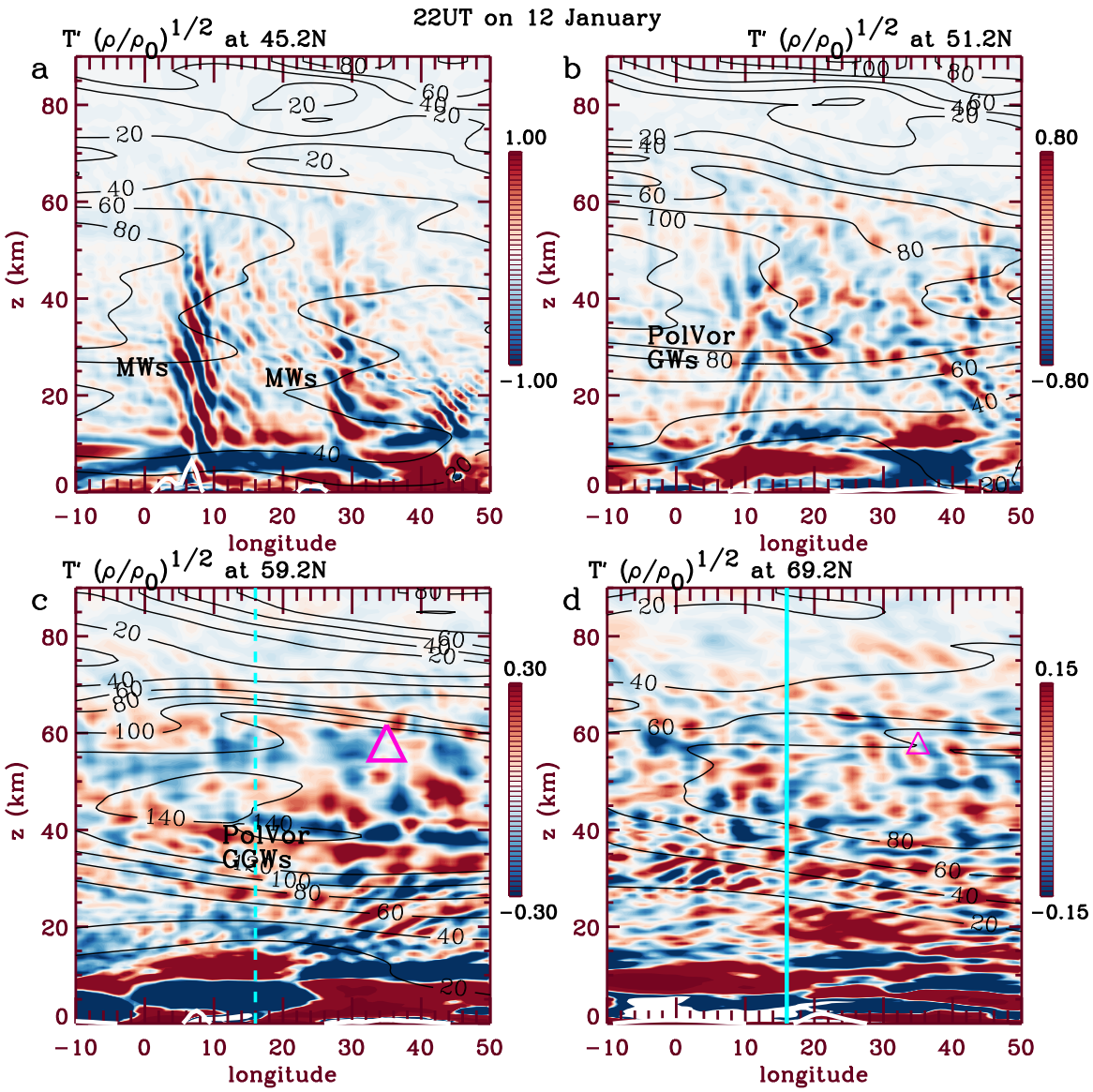

Figure 16. $T'\sqrt{\overline{\rho}/\rho_0}$ (colors, in K) at 22 UT on 12 January from the HIAMCM, where $\rho_0 = 1241\,\mathrm{g/m^3}$. (a) 45.2° N. (b) 51.2° N. (c) 59.2° N. The purple triangle shows the event #1 LBF and the dashed turquoise line shows the longitude of ALOMAR. (d) 69.2° N. The turquoise line shows ALOMAR and the small purple triangle shows longitude of the event #1 LBF. Black lines show U_{tot} (in m/s). White lines at the lower boundary show the height of the Earth's surface (in km) times 5. Labels show MWs and GWs generated by the polar vortex ("PolVor"). The colors are oversaturated to better see the GWs at $z > 15$ km.

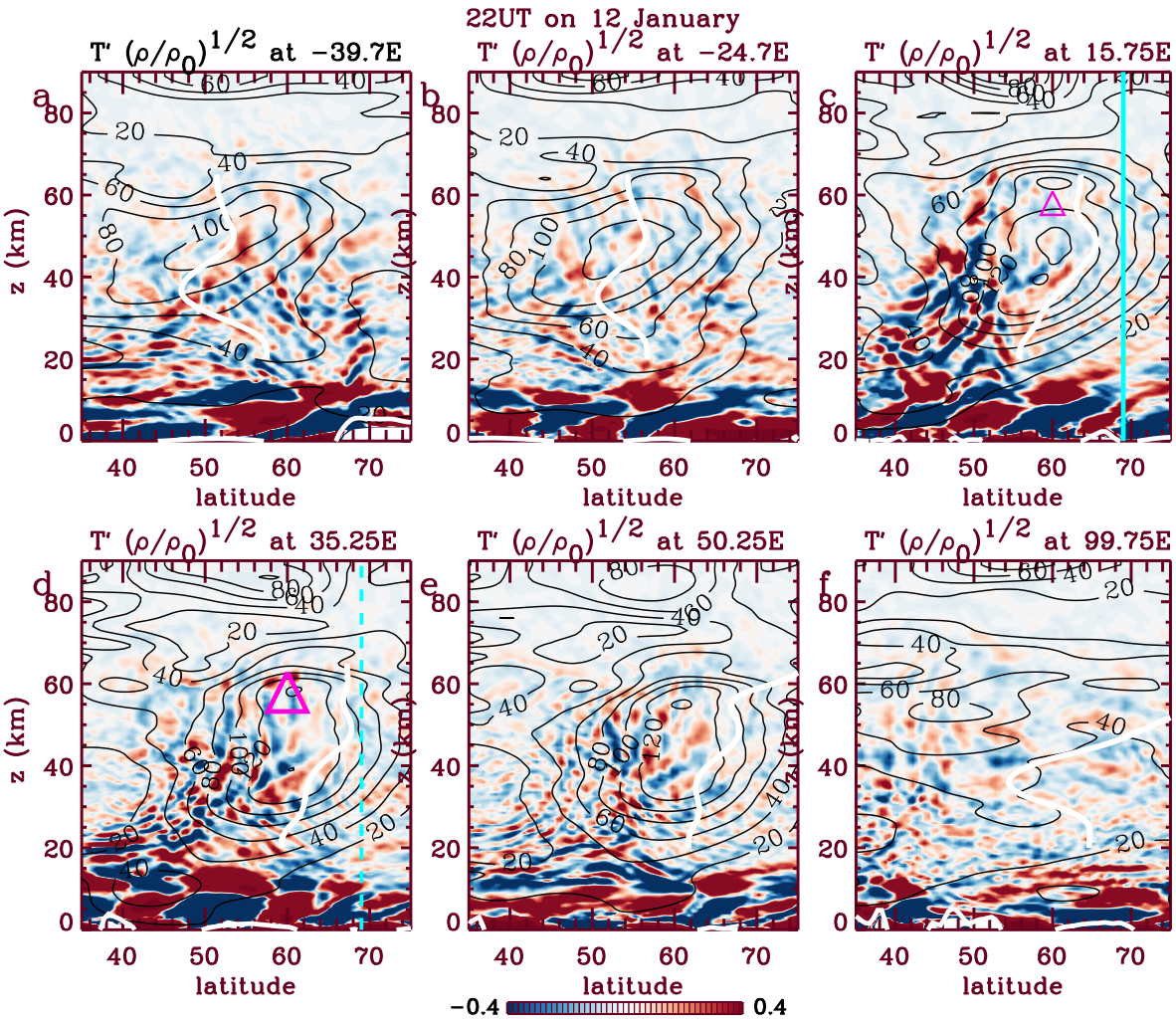

Figure 17. $T'\sqrt{\overline{\rho}/\rho_0}$ (colors, in K) at 22 UT on 12 January from the HIAMCM, where $\rho_0 = 1241\,\mathrm{g/m^3}$. (a) 39.7° W. (b) 24.7° W. (c) 15.8° E. The turquoise line shows ALOMAR and the small purple triangle shows the latitude of the event #1 LBF. (d) 35.3° E. The dashed turquoise line shows the latitude of ALOMAR and the purple triangle shows the event #1 LBF. (e) 50.3° E. (f) 100° E. Black lines show U_{tot} (in m/s). White lines at the lower boundary show the height of the Earth's surface (in km) times 5. White lines show the vortex edge. The colors are over-saturated to better see the GWs at $z > 15$ km.

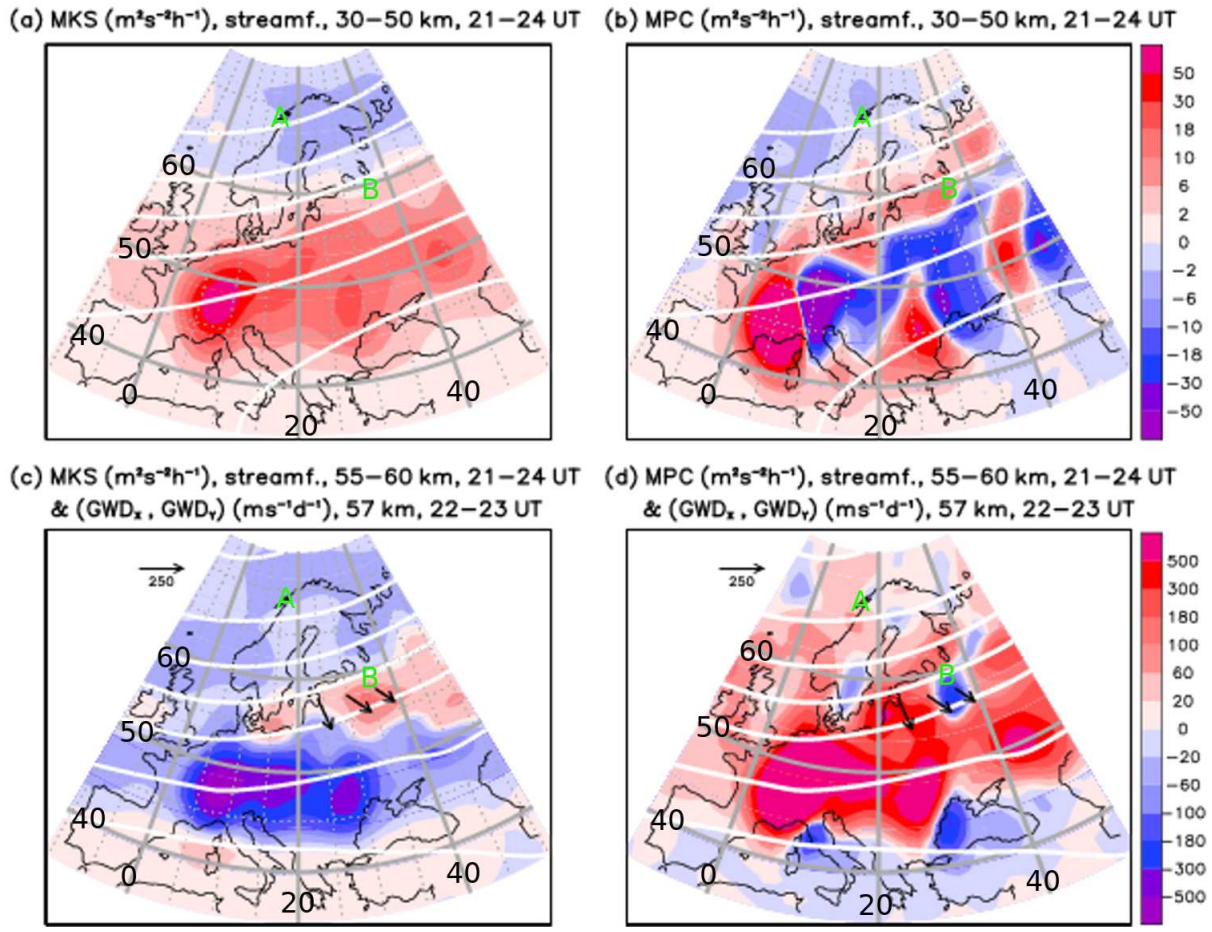

Figure 18. (a) Horizontal plot of the mesoscale kinetic energy source (MKS, colors, in $m^2/s^2/h$) averaged from $z = 30 - 50$ km and $21 - 24$ UT on 12 January for GW perturbations with $\lambda_H < 1350$ km. White contours show the correspondingly averaged horizontal streamfunction with intervals of 5×10^7 m^2/s. Grey lines show 0°, 20° and 40°E and 40°, 50° and 60°N, as labeled. (b) Same as (a), but for the mesoscale potential energy flux convergence (MPC) (colors, in $m^2/s^2/h$). (c),(d) Same as (a),(b), but averaged from $z = 55 - 60$ km. Black arrows show the horizontal body force (momentum deposition) vectors averaged from 22-23 UT at $z = 57$ km and 57.75°N for 24°, 30° and 36°E. ALOMAR and the event #1 LBF are labeled in green as "A" and "B", respectively. The black arrows in the upper left of panels c)-d) show 250m/s/day vectors.

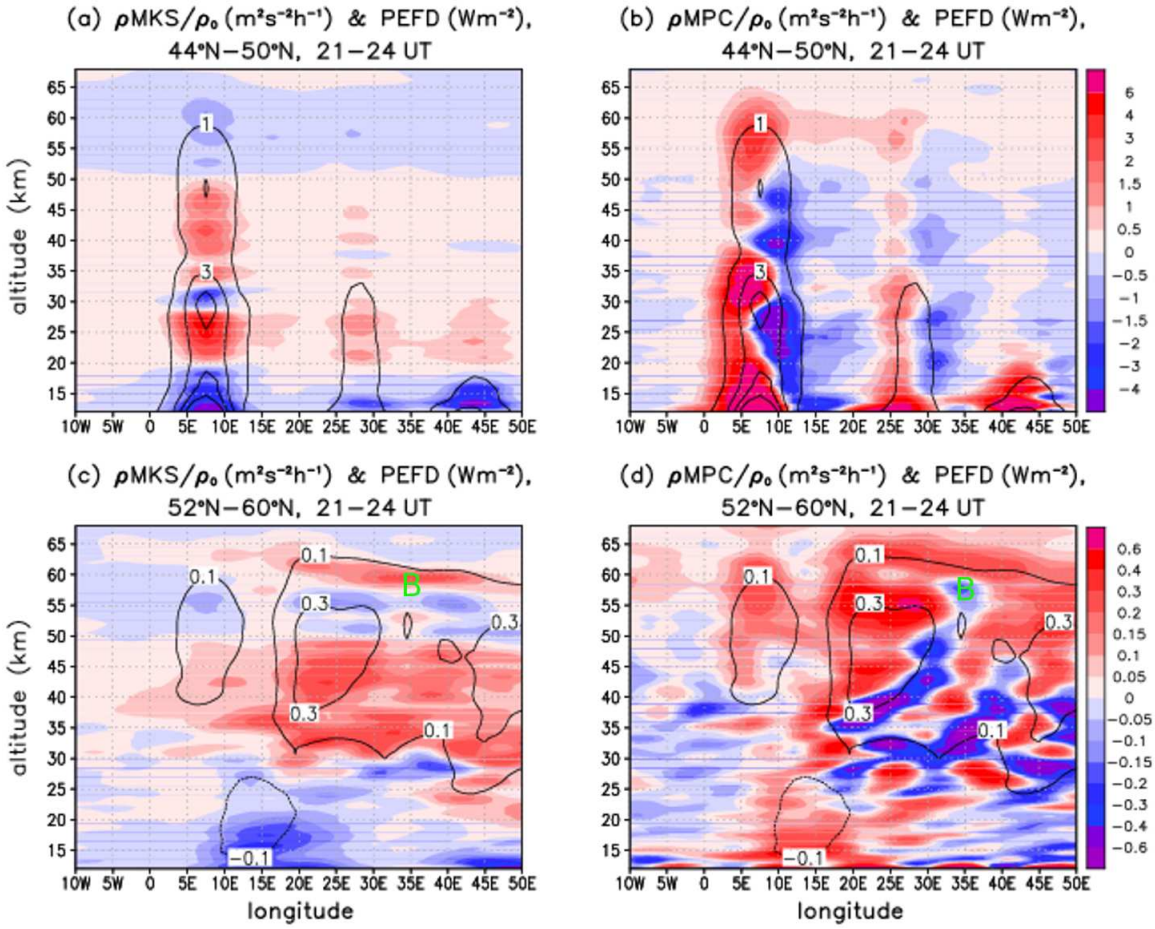

Figure 19. (a) Density weighted mesoscale kinetic energy source ($\overline{\rho}$ MKS/ρ_0, colors, in $m^2s^{-2}h^{-1}$) and mesoscale vertical potential energy flux density (PEFD, black contours in Wm^{-2}) as functions of longitude and altitude for perturbations with $\lambda_H < 1350$ km. Fields are averaged from $44-50°$N and 21-24 UT on January 12. PEFD corresponds to $\overline{p'w'}$, where p' and w' are the pressure and vertical velocity perturbations in the $z-$coordinate system. ρ_0 is the average density at $z = 12$ km. (b) Same as (a), but for the mesoscale potential energy flux convergence ($\overline{\rho}$ MPC/ρ_0, colors, in $m^2/s^2/h$). (c),(d) Same as (a),(b), but averaged from $52-60°$N. The event #1 LBF is labeled in green as "B", respectively, in c-d).

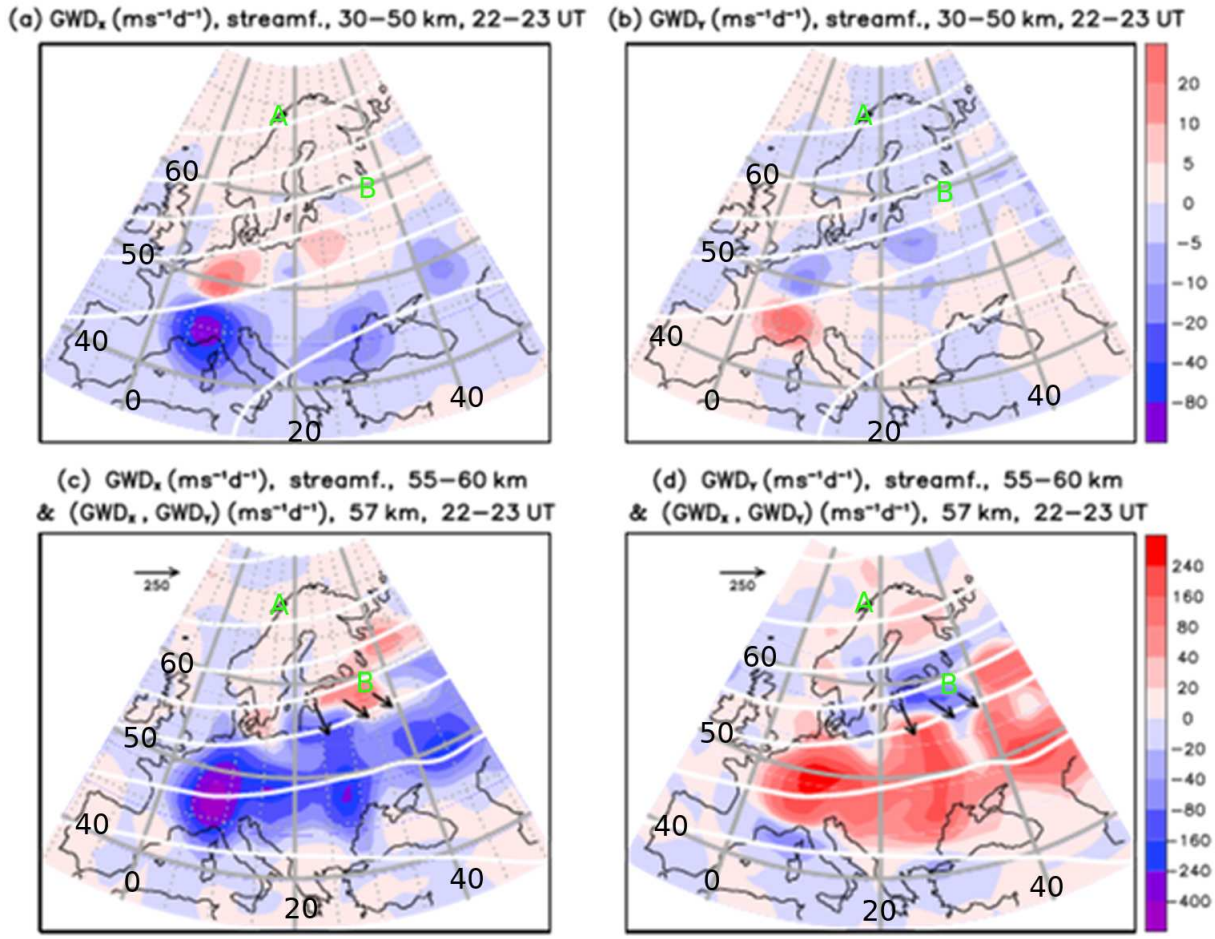

Figure 20. (a) Zonal GW drag (GWD_x) and (b) meridional GW drag (GWD_y) (colors, in m/s/d) averaged from $z = 30 - 50$ km and $22 - 23$ UT on 12 January for perturbations with $\lambda_H < 1350$ km. White contours show the correspondingly averaged horizontal streamfunction with interval of 5×10^7 m^2/s. Grey lines show 0°, 20° and 40°E and 40°, 50° and 60°N, as labeled. (c),(d) Same as (a),(b), but averaged from $z = 55 - 60$ km. Black arrows are the same as in Fig. 18. ALOMAR and the event #1 LBF are labeled in green as "A" and "B", respectively.

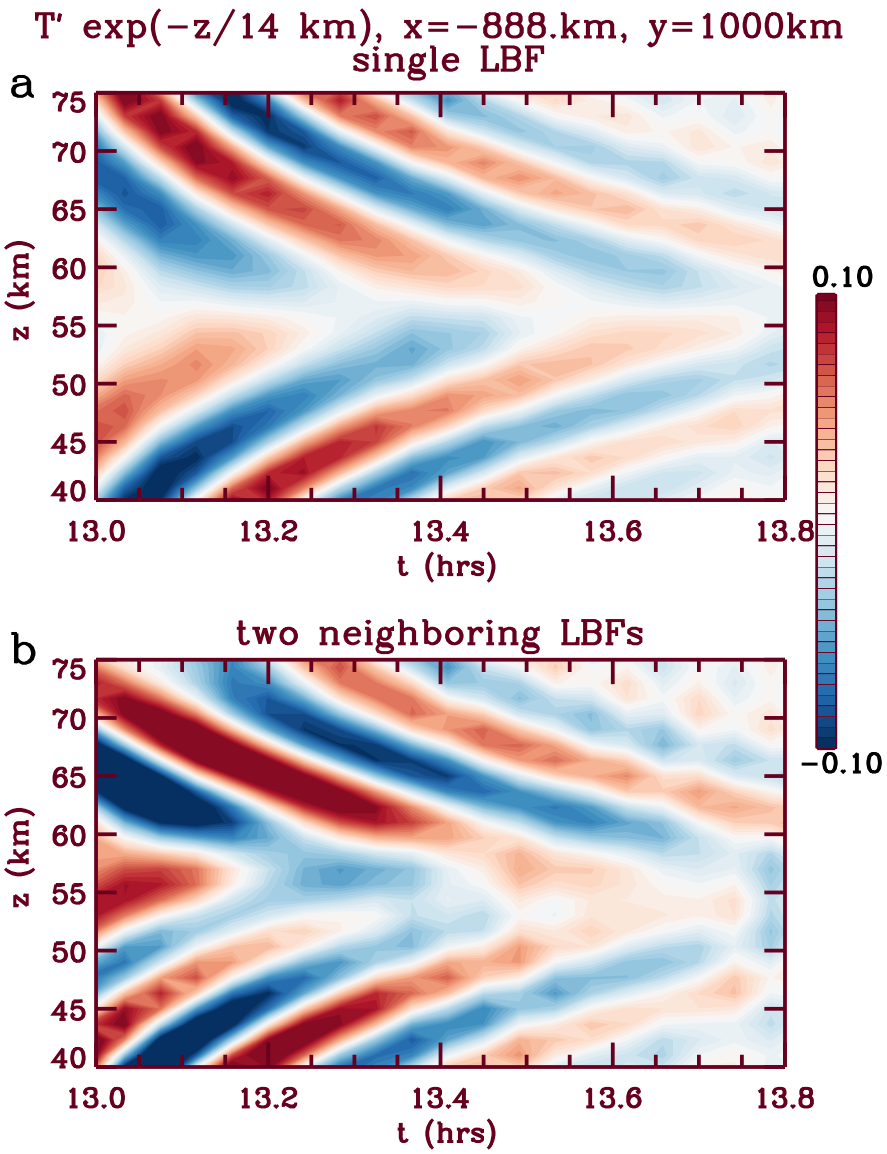

Figure 21. Theoretical fully compressible $f-$plane solutions of the secondary GWs excited by LBFs in an isothermal, windless atmosphere (see text). a) Height-time cross-section of $T'\exp(-z/14\text{km})$ (colors, in K) at ALOMAR (i.e., at $x = -888$ km and $y = 1000$ km) created from a LBF centered at $z_{\text{knee}} = 57$ km, 35° E and 60° N. b) Same as a), but for two neighboring LBFs. (x_0, y_0) is at the estimated event #1 LBF location of 35° E and 60°N. Note that the color scale is the same as in Fig. 8.

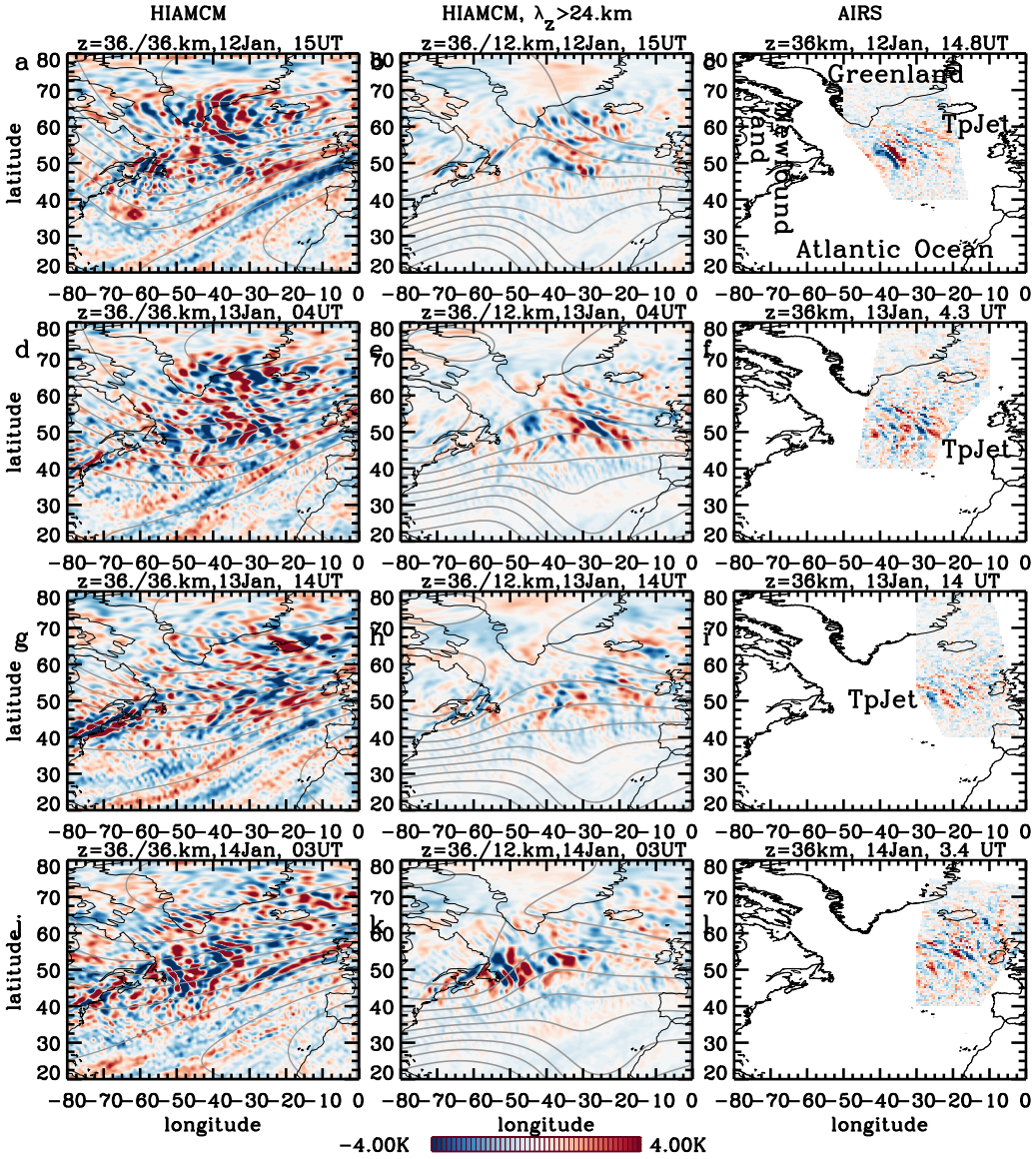

Figure 22. T' (colors, in K) at $z = 36$ km over the Atlantic Ocean. Row 1: 15 UT on Jan 12. Row 2: 4 UT on Jan 13. Row 3: 14 UT on Jan 13. Row 4: 3 UT on Jan 14. The left column shows the HIAMCM GWs and large-scale horizontal streamfunction at the same times and altitude (grey lines). The middle column is the same as the left column except 1) filtered to remove GWs with $|\lambda_z| < 24$ km, and 2) the stream function is shown at $z = 12$ km. The right column shows the AIRS GWs. Labels show the GWs generated by the tropospheric jet east of Newfoundland ("TpJet").